

## COLORS OF AGN HOST GALAXIES AT $0.5 < z < 1.1$ FROM GEMS

S. F. SÁNCHEZ<sup>1</sup>, K. JAHNKE<sup>1</sup>, L. WISOTZKI<sup>1,2</sup>, D. H. MCINTOSH<sup>3</sup>, E. F. BELL<sup>4</sup>, M. BARDEN<sup>4</sup>, S. V. W. BECKWITH<sup>5</sup>, A. BORCH<sup>4</sup>, J. A. R. CALDWELL<sup>6</sup>, B. HÄUSSLER<sup>4</sup>, S. JOGEE<sup>6</sup>, K. MEISENHEIMER<sup>4</sup>, C. Y. PENG<sup>7</sup>, H.-W. RIX<sup>4</sup>, R. S. SOMERVILLE<sup>6</sup>, C. WOLF<sup>8</sup>

(Dated: Received / Accepted)  
Draft version March 20, 2022

### ABSTRACT

We present the results from a study of the host galaxies of 15 optically selected AGNs with  $0.5 < z < 1.1$  from GEMS. GEMS is a Hubble Space Telescope imaging survey of a  $28^\circ \times 28^\circ$  contiguous field centered on the Chandra Deep Field South in the F606W and F850LP filter bands. It incorporates the SEDs and redshifts of 10 000 objects, obtained by the COMBO-17 project. We have detected the host galaxies of all 15 AGNs in the F850LP-band (and 13/15 in the F606W-band), recovering their fluxes, morphologies and structural parameters. We find that 80 % of the host galaxies have early-type (bulge-dominated) morphologies, while the rest have structures characteristic of late-type (disk-dominated) galaxies. We find that 25 % of the early types, and 30 % of the late types, exhibit disturbances consistent with galaxy interactions. The hosts show a wide range of colors, from those of red-sequence galaxies to blue colors consistent with ongoing star formation. Roughly 70 % of the morphologically early-type hosts have rest-frame blue colors, a much larger fraction than those typical of non-active morphologically early-type galaxies in this redshift and luminosity range. Yet, we find that the early-type hosts are structurally similar to red-sequence ellipticals, inasmuch as they follow an absolute magnitude versus half-light size correlation that are consistent with the mean relation for early-type galaxies at similar redshifts.

*Subject headings:* galaxies:active – galaxies: fundamental parameters – galaxies: starburst – quasars: general

### 1. INTRODUCTION

There is now a wide agreement that most if not all galaxies with bulges harbor massive black holes in their centers (e.g., Magorrian et al. 1998; Kormendy & Gebhardt 2001). However, only a fraction of the galaxies harbor a quasar-like active nucleus (AGN). AGNs are often seen as compact sources in the nucleus of galaxies, with strong highly-ionized broad and narrow emission lines. They are thought to be powered by a central supermassive black hole, fed by the accretion of gas from the inner 100 pc of the host galaxy (Antonucci 1993; Urry & Padovani 1995). While both a massive black hole and a reservoir of gas are believed to be important for triggering high level AGN activity, it is as yet unclear which conditions are needed to trigger such activity. Fundamental questions remain regarding the relationship between the AGN, its host galaxy, and star formation, the gas inflow rates needed to fuel the nuclear source, and the relevant fueling mechanisms on different physical scales. The morphology and spectral properties of AGN host galaxies over different redshift regimes can bring important insights to these issues.

According to the currently favoured view, galaxy-galaxy interactions or mergers are important mechanisms for (re-

igniting AGN (e.g., Canalizo & Stockton 2001), except perhaps for very low-level nuclear activity (e.g., Collin et al. 2003; Ho 2003). Mergers and interactions can induce large-scale radial motion of the interstellar gas within the AGN host, and trigger its infall into the inner regions to be accreted at later times by the AGN. Sanders et al. (1988) first proposed an evolutionary scenario in which galaxy encounters could produce ultraluminous infrared galaxies (ULIRGs), that would evolve into AGNs. This hypothesis is supported by several studies which found a large fraction of merger/interacting systems in the hosts of high-luminosity AGNs (e.g. Bahcall et al. 1995, 1997; Hutchings & Neff 1997; Canalizo & Stockton 2001; Sánchez & González-Serrano 2003). Yet, Dunlop et al. (2003) have not found merger/interactions in their sample of low- $z$  AGNs. An important limitation of these previous studies is the lack of a well-defined comparison sample of inactive galaxies, whose data were obtained and analyzed in similar way to the active ones.

A severe practical problem for the study of the hosts of AGNs is the presence of the bright nucleus, which has to be carefully removed. This strong point-like source, as bright or even brighter than the galaxy, contaminates the host flux in all the areas covered by the point spread function (PSF). It also reduces the SNR (signal-to-noise ratio) within the host. This affects strongly the reliability of any morphological classification of the host. Consequently, ground-based studies are normally limited to low-redshift ( $z < 0.5$ ), where the typical size of the host is larger than the seeing disc (e.g. Dunlop et al. 1993; Taylor et al. 1996; McLeod & Rieke 1994, 1995; Jahnke & Wisotzki 2003), or to wavelength ranges where the host emission dominates the AGN (e.g., near-infrared), increasing the contrast (e.g. Dunlop et al. 1993; McLeod & Rieke 1994; Falomo et al. 2001; Sánchez & González-Serrano 2003). The use of HST imaging has clearly increased our understanding of the host properties, reducing the effects of contamination from the nu-

<sup>1</sup> Astrophysikalisches Institut Potsdam, An der Sternwarte 16, 14482 Potsdam, Germany

<sup>2</sup> Universität Potsdam, Am Neuen Palais 10, 14469 Potsdam, Germany

<sup>3</sup> Department of Astronomy, University of Massachusetts, 710 North Pleasant Street, Amherst, MA 01003, USA

<sup>4</sup> Max-Planck-Institut für Astronomie, Königstuhl 17, 69117 Heidelberg, Germany

<sup>5</sup> Space Telescope Science Institute & Johns Hopkins University, 3700 San Martin Drive, Baltimore MD, 21218, USA

<sup>6</sup> Space Telescope Science Institute, 3700 San Martin Drive, Baltimore MD, 21218, USA

<sup>7</sup> Steward Observatory, University of Arizona, 933 N. Cherry Ave., Tucson AZ, 85721, USA

<sup>8</sup> Department of Physics, Denys Wilkinson Bldg., University of Oxford, Keble Road, Oxford, OX1 3RH, UK  
Electronic address: ssanchez@aip.de

TABLE 1  
PROPERTIES OF THE GEMS LOW- $z$  AGN SAMPLE

QSO ID	Tile	$z^1$	R-band	F606W-band	F850LP-band
34357	94	<i>0.543</i>	18.73	19.22	0.06
41310	47	0.548	23.09	23.24	0.09
41310	40	0.548	23.09	23.20	0.09
52963	50	0.548	22.69	22.72	0.09
36361	94	0.549	22.50	23.39	0.09
47615	46	0.649	22.28	22.08	0.08
50415	85	<i>0.664</i>	22.39	22.75	0.09
50415	51	<i>0.664</i>	22.39	22.74	0.09
44126	42	0.729	23.03	23.04	0.09
42601	42	<i>0.733</i>	21.02	21.32	0.08
48284	85	<i>0.734</i>	19.05	19.33	0.06
39432	89	<i>0.738</i>	22.02	22.16	0.08
31898	30	0.812	22.91	23.10	0.09
15731	18	0.835	20.11	19.77	0.07
50997	85	<i>0.837</i>	20.43	20.60	0.07
50997	51	<i>0.837</i>	20.43	20.43	0.07
49298	52	<i>1.031</i>	19.92	19.89	0.07
49298	85	<i>1.031</i>	19.92	19.90	0.07
43151	95	<i>1.037</i>	22.18	22.25	0.08
43151	45	<i>1.037</i>	22.18	22.38	0.09

<sup>1</sup> values in italics are spectroscopic redshifts obtained from Szokoly et al. (2004).

cleus due to the very narrow intrinsic PSF (e.g. McLure et al. 2000; Pagani et al. 2003). However, most published HST host studies were based on WFPC2 imaging with short exposures due to the high AGN flux, with a limited determination/treatment of the PSF.

An additional limitation of previous studies has been the sample selection. Several samples have been selected *ad hoc*, for testing specific hypotheses (e.g., Dunlop et al. 1993; Canalizo & Stockton 2001). Other samples are based on unclear selection criteria (e.g., Hutchings & Neff 1992; Bahcall et al. 1995) or are clearly incomplete and/or statistically small (e.g., Hutchings & Neff 1997). In some cases the images were not deep enough for an accurate morphological analysis (e.g., Lehnert et al. 1999). A few studies are based on statistically significant, flux-limited samples (e.g., Jahnke et al. 2004; Jahnke & Wisotzki 2003), although the results from these studies are limited by the lack of a similarly selected comparison sample of inactive galaxies.

All these difficulties can be better addressed by the *Galaxy Evolution from Morphology and SEDs* project (GEMS, Rix et al. 2004), where AGNs have been identified by the COMBO-17 multi-color survey (Wolf et al. 2003). We have selected the 15 AGNs with  $0.5 < z < 1.1$  from GEMS, coincident with the best studied redshift range for the inactive galaxies in that survey. Using an accurate determination of the PSF, and a two-dimensional (2D) fitting technique, we decouple the host and nuclear components in these objects, and compare the properties of the host galaxies with those of inactive galaxies.

The sequence of this article is as follows. In Section 2 and 3 we describe the data and the data analysis. In Section 4 we present the results, and we discuss these in Section 5. The summary and conclusions are presented in Section 6. Throughout this article we assume a  $\Lambda$ -cosmology, with  $H_0 = 70 \text{ km s}^{-1} \text{ Mpc}^{-1}$ ,  $m = 0.7$  and  $\Omega = 0.3$ . We have used the AB photometric system for the observed magnitudes and colors, and the Vega system for the rest-frame colors and absolute magnitudes, unless explicitly stated otherwise.

## 2. THE DATA

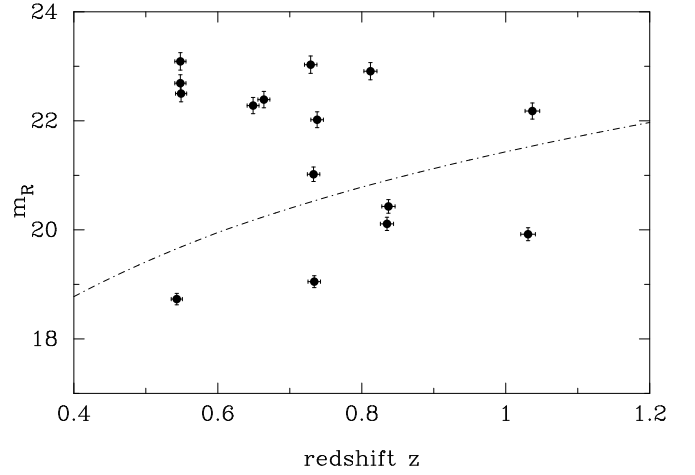


FIG. 1.— R band magnitudes of the AGN sample as measured in COMBO-17, plotted against COMBO-17 redshift. The dot-dashed line corresponds to constant  $M_B = -23$  for the mean quasar SED of Elvis et al. (1994).

GEMS is a two band, F606W and F850LP (similar to the V and z-bands), HST imaging survey covering 78 pointings using the ACS camera. This survey covers a continuous field of  $28^\circ \times 28^\circ$  in the extended Chandra Deep Field South, to a depth of F606W = 28.3 (5  $\sigma$ ) and F850LP = 27.1 (5  $\sigma$ ) for compact sources. In its central  $1/4$ , GEMS incorporates ACS imaging from the GOODS project (Giavalisco et al. 2004). Only the first epoch coverage from GOODS was used, resulting in images that are considerably shallower than the final GOODS data, but also slightly less deep than the surrounding proper GEMS tiles. The full GEMS data reduction will be described elsewhere (Caldwell et al., in preparation). It comprises the standard data reduction (bias subtraction, flat-fielding, flux calibration), drizzling of the data from the original  $0''.05/\text{pixel}$  to a final sampling of  $0''.03/\text{pixel}$ , background estimation and variance determination for each pixel. As the deblending of nuclear and host galaxy components with two-dimensional modelling (the main purpose of this article) is sensitive to background errors, we applied an extra procedure to remove local background residuals. This includes an iterative masking of all objects in the field and the determination of the local background from the object-free regions. For each area of  $200 \times 200$  pixels an average from the unmasked pixel was computed, with a subsequent bilinear interpolation between these values to yield a background estimate for the whole field. The overall properties (pixel size, noise pattern, etc.) of the images in both passbands are quite similar, although the F606W images are deeper by 1 mag.

The GEMS area has been previously studied by COMBO-17, a photometric redshift survey based on imaging in 12 medium and 5 broad-band filters (Wolf et al. 2003). GEMS incorporates the redshift and spectral energy distribution (SED) classifications of 10 000 objects from COMBO-17, including a sample of 120 AGNs with  $0.5 < z < 5$ . Because of the SED-based selection technique within COMBO-17, most of these AGNs are type I, i.e., they show broad emission lines. We introduced a cut at  $m_R < 24$  Vega mag for SED and redshift reliability, defining a subsample of 80 objects. For the redshift range of our interest ( $0.5 < z < 1.1$ ), this cut defines a subsample of 18 AGNs, and limits the uncertainty of the COMBO-17 redshift to  $z \pm 0.02$ . In a final cleaning pass of the sample we excluded, by visual inspection,

tion, those objects located at the very edges of the tiles. The final sample comprises 60 AGNs with accurate redshift and good imaging, 15 of them at  $0.5 < z < 1.1$ . Most of the finally selected objects have absolute magnitudes of around or just below  $M_B = -23$ , which for an Einstein-de Sitter universe with  $H_0 = 50 \text{ km s}^{-1} \text{ Mpc}^{-1}$  corresponds to the conventional division between high-luminosity QSOs and lower luminosity Seyferts, Schmidt & Green (1983).

This sample allows us, for the first time, to study a complete flux-limited sample of AGN hosts, with a similarly-selected and studied inactive comparison sample. We have extracted postage-stamp images of  $128 \times 128$  pixels size ( $3''.84 \times 3''.84$ ) of the F606W and F850LP-bands, centered on each AGN.

The redshift range has been selected for several reasons. The main aim of this selection is that the F606W and F850LP-band sample two physically distinct spectral ranges. While the F606W-band always samples the wavelength range bluewards of the Balmer break ( $\sim 4000\text{\AA}$ ), and is therefore sensitive to OB stars in the galaxies, the F850LP-band lies entirely redwards of this break, probing the old population of red stars in the galaxies. The F606W–F850LP colors will therefore allow us to explore the degree of star formation activity in a homogeneous way for the entire sample. The angular scales between  $z = 0.5$  and  $1.0$  change only by a factor 1.5, and cosmological surface brightness dimming is not yet a major effect. Therefore, this selection allows us to perform a structural analysis in a homogeneous way to all objects. Finally, this redshift range coincides with the peak of the GEMS redshift distribution, enabling us to access a large and well-defined comparison sample. In a separate article we study the host galaxy properties of GEMS AGN at much higher redshifts,  $1.8 < z < 2.75$  (Jahnke et al. 2004).

Table 1 gives a summary of the properties of the AGNs of our sample, including the COMBO-17 ID, the GEMS tile of the analyzed image, the redshift and R-band photometry from COMBO-17 and the F606W and F850LP-band photometry from the GEMS data. Whenever available, we have used the spectroscopic redshifts obtained by Szokoly et al. (2004) in their optical study of the X-ray sources in the Chandra Deep Field South (redshifts in italics in table 1). The spectroscopic and COMBO-17 redshifts agree within the expected errors (for a full discussion of redshift accuracy in COMBO-17 see Wolf et al. (2004)). Five of the 15 AGNs are located in overlapping tile areas and thus received double exposure times. We have analyzed each individual image and compared the results at the end. Figure 1 shows the distribution of (COMBO-17 based) R-band Vega magnitudes as a function of redshift.

### 3. ANALYSIS OF THE DATA

There are various problems in the detection and restoration of the hosts of AGNs. Most of them relate to the presence of the AGN itself, a strong point-like source that, due to the PSF, contaminates the host image. The level of contamination depends on the contrast (the flux ratio between the nucleus and the extended component), the overall SNR, and the accuracy of the PSF determination. Here, we present the method used to detect and characterize the AGN hosts, and to estimate the uncertainties.

#### 3.1. PSF production

An extensive study of the ACS PSF based on GEMS data will be presented elsewhere (Jahnke et al., in preparation). On the basis of this study, we find that the PSF shape varies across the ACS field-of-view, with pixel-to-pixel flux variations .

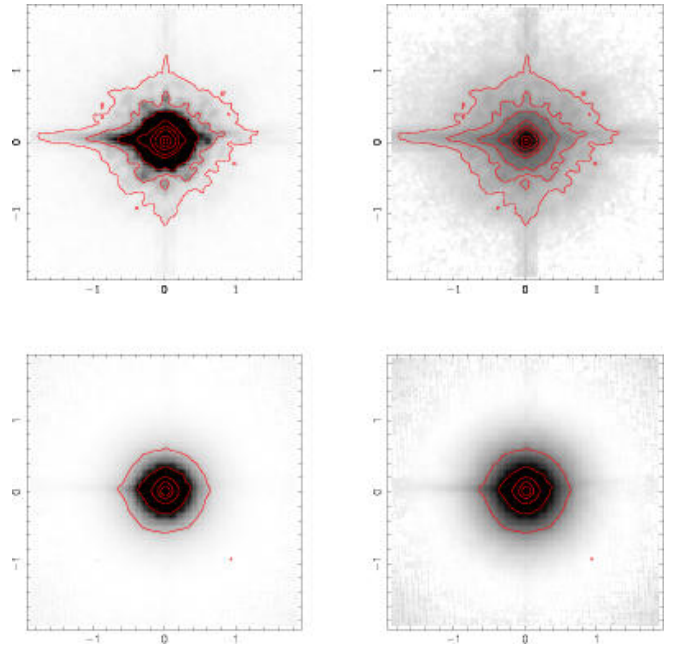


FIG. 2.— Average PSF over the whole GEMS field for the F850LP-band, plotted in linear (top-left) and logarithmic scales (top-right). The variance map of the PSF is also plotted, in linear (bottom-left) and logarithmic scales (bottom-right). The contours are plotted in logarithmic scale, starting at  $10^{-5}$  counts for the 1st contour and with a separation of 0.5 dex.

20 %. This prevents us from using a single mean PSF for our analysis. We find that temporal variations are negligible compared to spatial variations. Therefore, we built a local PSF around the position of each AGN, averaging the nearest 35 isolated stars within a distance of  $40''$ . In order to take the uncertainties of the PSF determination into account for later image modelling, we included these uncertainties in the total pixel variance budget. Figure 2 shows the mean PSF averaged over the whole GEMS field, plotted in both a linear and a logarithmic scale to show the spikes and substructures. We also show the variance map of the global mean PSF; each individual PSF has a similar associated variance map which was used in the fitting process.

#### 3.2. Simple PSF subtraction

A simple method for the detection of the hosts was applied by subtracting the PSF scaled to the QSO peak intensity: the PSF was scaled to the central flux of the AGN, integrated inside a circular aperture of 4 pixels ( $0''.12$ ) diameter centered on the nucleus, and then subtracted from the AGN. This method is very conservative with respect to the host galaxy detection since it implies, by definition, an oversubtraction of the nuclear component from the inner regions. It provides us with a non-model-dependent detection and a lower limit on the host flux. In order to quantify the results from this detection method we tested it using 200 field stars, covering a magnitude range similar to our objects. We find false detections of a host contributing more than a 10 % (5 %) to the total flux in only 3 % (12 %) of the field stars. Here we will assume a *hard* lower limit of 10 % of the total flux for a reliable host detection. We expect no spurious detections in our sample of 15 objects with this adopted limit.

Applying this method, we have detected hosts in all the 15 objects for the F850LP band, and in 13 of the 15 AGNs for the F606W band images. The two objects not detected

in the F606W-band, COMBO-17 50997 and COMBO-17 43151, are both at a relatively high redshift. Their hosts are clearly detected in the F850LP-band, being most likely compact spheroids (as we will discuss below). Fortunately, both objects were observed by GEMS and GOODS, being in an overlapping region. In this case we have combined the images obtained from both projects, and applied the subtraction analysis. We have found some residuals in the images, especially for COMBO-17 50997, coincident with the F850LP-band residuals by a visual inspection. However, they are still below the reliability criteria and we disregard these weak residuals in what follows.

### 3.3. 2D modeling

We performed two-dimensional modelling of the images to recover more accurately the nuclear and host fluxes, and to determine some morphological parameters of the hosts. The fitting was performed using GALFIT v1.7a (Peng et al. 2002). This software fits galaxy images with a 2D model, which consists of a superposition of parametrized fitting functions for point-like and extended sources. A fitting process then optimizes the flux scaling factors and morphological parameters such as scale lengths, ellipticities and position angles, by means of  $\chi^2$  minimization operating on the original pixel data.

The AGN images were fitted with a two-component model: a Gaussian function with a very narrow width for the nuclear component (a quasi-delta function) and a galaxy model for the host. The FWHM of the Gaussian was fixed to the average value obtained from the fit with a single Gaussian to the stars used to create the PSF. Nearby companions were masked before performing the fitting. We did not preselected a certain galaxy model (disk or spheroid) for our objects, since the morphological determination was one of the goals of this study. Instead, we assumed that the hosts could be characterized by either of two single models: (1) an exponential disk (Freeman 1970) for disk-dominated galaxies, or (2) a de Vaucouleurs  $r^{1/4}$  function (de Vaucouleurs & Capaccioli 1979) for bulge-dominated galaxies. Due to the complexity of the problem, we did not try to decouple the disk from the bulge, which would have required a third fitting function into the model. We also performed a fit to characterize the host galaxy as a Sersic function (Sersic 1968), which helped in establishing a morphological classification as shown below.

The 2D fit provided us with a robust method to decouple the nucleus and the host, allowing us to obtain the fluxes of both components. For each model, the nucleus image was subtracted from the original image, to provide a complete image of the host, including its substructures. We have obtained the total flux of the host by direct measurement of this *restored* image.

Finally, we also performed a surface brightness (SB) profile analysis of the images, fixing the ellipticity and the position angle to the values obtained from the 2D fitting. The SB profiles were used to visually check the results from the 2D modelling. The physical scale and the surface brightness of the galaxies were estimated measuring the half-light radius ( $r_{1/2}$ ) and the SB at this radius ( $\mu_{1/2}$ ).

Tables 2 and 3 summarize the results of this analysis. For the images of each object we list the model of the host included in the fitting (disk, de Vaucouleurs or the Sersic index derived from the fitting), the derived total, nuclear and host galaxy magnitudes from the model, the host-to-nuclear flux ratio (H:N), the axis ratio of the host (a/b), the position angle (PA) and the reduced  $\chi^2$  of the fit. We also provide the mag-

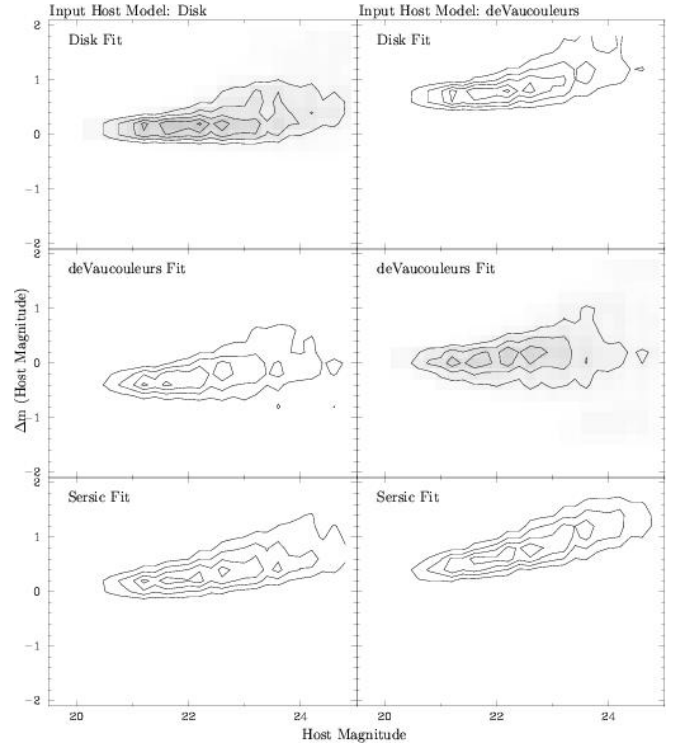


FIG. 3.— Density distribution of the differences between the input and the output magnitudes of the host galaxies for the two simulated models (disk and de Vaucouleurs), when fitted with three different functions: exponential disk, de Vaucouleurs and Sersic, as described in the text. The first contour encircles 90 % of the objects, with a separation of 20 % between each successive contours.

nitude derived from the peak-scale PSF subtraction described above (Sub), the magnitude of the *restored* host image (Emp) together with the half-light radius and surface brightness.

### 3.4. Limits of the method: simulations

To understand the limitations of our methodology we performed simulations. We created simulated images that mimic, as much as possible, the real data. Due to the large similarities between our F606W and F850LP images, we simulated only F850LP images, and translated the results to F606W by a simple zero-point shift transformation ( $F606W_0 - F850LP_0 = 1.6502$  mags). The AGNs were simulated with a two component model (nucleus+host), plus noise. The nucleus was simulated by a scaled PSF, using the mean PSF shown in Figure 2. The host galaxy was simulated using a single model, either an exponential disk or a de Vaucouleurs function. Clearly this was an oversimplification of the true diversity in galaxy morphological types. However, most of our objects can be clearly classified as either bulge- or disk-dominated (see below), with very few cases of ambiguous morphological type. The simple dichotomy assumed in the simulations is therefore appropriate for the purpose of this paper.

To reproduce the noise pattern seen in the real images, due to the drizzling process on the reduction (Caldwell et al., in preparation), we created the noise map in two steps. A first guess of the noise map was built using the noise-free simulated images, assuming a Poisson distribution for the noise, and adding the noise due to the background and readout noise. Due to the drizzling the noise distribution of the real images is narrower than that expected from Poissonian statistics, and

there are correlations between neighboring pixels. In order to simulate this noise pattern we smoothed the simulated noise images by a mean filter using a  $3 \times 3$  pixels box. Then we combined this smoothed noise map with the original Poissonian one, with different relative weights, until recovering the observed noise distribution. The final noise map consisted of 80% of the original map plus 20% of the smoothed one.

We covered a wide range of parameter space in our simulations, going outside the expected boundaries for real data to explore possible systematic effects. The simulations range in total magnitudes between 18.5 and 25.5, with a range of host-to-nucleus flux ratios between 0.1 and 2.0 (9–66 % of the total flux), and half-light radii for the hosts between  $0''.15$  and  $1''.0$  (between 0.5 and 10 kpc at the redshift of our objects). For each set of data we created five different realizations, based on different noise maps. We finally created a total of 1880 simulated AGN, 940 pairs with similar parameters, but different host morphologies. The simulated images were created both by the GALFIT and IRAF/ARTDATA packages, without significant differences in the final results.

With these simulations we explored the range of parameter space for which our method could robustly reclaim the key parameters (total, nucleus and host fluxes, host scale length, and the contrast between host and nucleus). We also searched for possible biases in the derived parameters, and we estimated statistical errors by comparing the input and output values. To place limits on our ability to differentiate between disk-dominated and bulge-dominated galaxies, we fitted all the simulations, like the real data, with three different models for the host galaxy: An exponential disk, a de Vaucouleurs function, and a Sersic function (with a free  $n$ -index). The total number of performed fits was 5640. A detailed description of these simulations will be presented elsewhere (Sánchez et al, in preparation), here we give only a brief summary. In all cases we find that the nuclear magnitude is recovered with higher accuracy than the host magnitude. Figure 3 shows the distribution of the difference between the input and output host magnitudes versus the input magnitudes, for the different input and fitted models. It is clear from this figure that the best estimation of the host magnitude depends on an accurate assessment of the host morphological type.

The error in total and nuclear magnitudes is always lower than  $0.12$  magnitudes. On the other hand, the accuracy of host magnitudes depend more on the host flux (SNR) than on other parameters like the contrast (host-to-nucleus ratio), or the host physical scale (for  $r_{1=2} > 0''.15$ ). The flux of the disk hosts is better recovered than the flux of the elliptical hosts for the same range of parameters. This is due to the ACS PSF following roughly an  $r^{1=4}$ -profile (Jahnke et al., in preparation), which makes it more difficult to disentangle nuclear point sources from spheroidal than from disk host. Another reason could be that disk galaxies are less concentrated, and therefore, for the same luminosity, they have more light in the wings. The error of the host magnitudes ranges from  $0.05$  mag for the brightest disk hosts ( $F850LP_{\text{host}} \approx 20$ ) to  $0.40$  mag for the faintest spheroidal hosts ( $F850LP_{\text{host}} \approx 24$ ).

It has already been noted (McLure et al. 1999; Sánchez & González-Serrano 2003) that it is not possible to perform an accurate morphological classification of host galaxies based simply on the goodness of the fit to either disk or de Vaucouleurs models (i.e., a comparison of the reduced  $\chi^2$ ). The model fitting is dominated so strongly by the nucleus fitting that the derived goodness parameter is

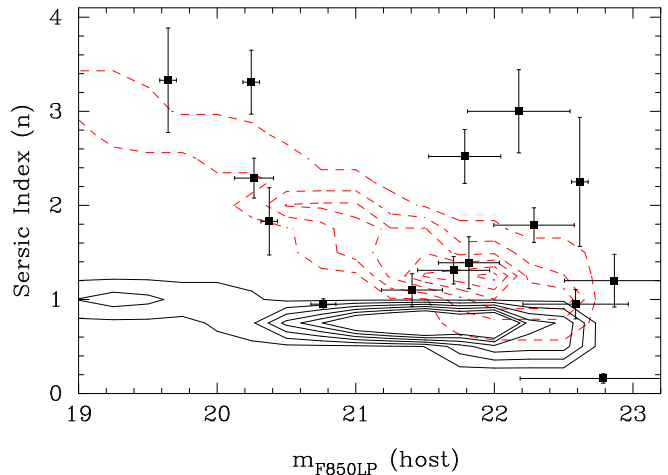


FIG. 4.— Density distribution of the output Sersic index from 2D fitting to simulated disk ( $n = 1$ , solid line) and de Vaucouleurs ( $n = 4$ , dotted line) host galaxies. The outer contour encircles 95 % of the simulations, with increments of 15% between successive contours. The solid squares show that distribution for the host galaxies of our AGN sample (values listed in table 3).

similar for both models (Sánchez & González-Serrano 2003). However, we find that we achieve a reliable morphological classification using the Sersic index from our fitting and comparing this to the results of our simulations. In absence of the nucleus and without noise, the Sersic index should be 1 for a pure disk model and 4 for a pure de Vaucouleurs model. The presence of the nucleus and the noise alters this result. This classification method was already used by McLure et al. (1999) and Sánchez & González-Serrano (2003).

Figure 4 shows the distribution of the output Sersic indices along the simulated host magnitudes for the input disks (solid contours) and the input de Vaucouleur spheroids (dashed contours). The Sersic indices are close to their input values only for very bright host galaxies and tend to become smaller as a consequence of the presence of a central point source. Nevertheless, the two classes of disk and de Vaucouleurs models remain well separated unless the host galaxy is very faint. Based on these simulations we conclude that we can perform a reliable morphological classification at least into disk- or spheroid-dominated types for most of our objects.

#### 4. RESULTS

Based on our fitting analysis and the simulations, we assigned a morphological class to each of the AGN hosts (Tables 2 and 3). We selected the morphological type for each host galaxy by comparing its location in the Sersic index vs. host magnitude plane with the distribution obtained from the simulations (Fig. 4). This way, we derived initial morphological classifications for each filter band separately. If an object was observed more than once, in different mosaic tiles (see Tables 2 and 3), we used the average value of the two Sersic indices. If one of the two images originated in the GOODS area, we gave preference to the values derived from the analysis of the GEMS tile (since the GOODS tiles incorporated into GEMS are slightly shallower than the proper GEMS tiles, cf. Sect. 2). From these criteria we could obtain unambiguous classifications for 11 of the 15 objects, of which 9 have the same type in both bands, and 2 were detected only in F850LP. All these 11 objects are located in a non-overlapping region between the spheroid and disk distri-



TABLE 2  
RESULTS FROM THE 2D FITTING: F606W-BAND IMAGES

QSO ID	Tile	Model	Tot	Nuc	Host	H:N	a/b	P.A.	<sup>2</sup>	Sub	Emp	r <sub>1=2</sub>	r <sub>1=2</sub>
34357	94	disk	19.29	19.51	21.15	0.22	0.87	15.27	1.57	21.70	21.96	0.52	23.20
		deVauc	19.19	19.53	20.63	0.36	0.92	18.55	1.57	21.70	21.82	0.52	23.36
		1.76	19.27	19.53	20.96	0.26	0.89	16.15	1.56	21.70	21.86	0.52	23.27
41310	47	disk	23.32	23.91	24.27	0.71	0.52	44.38	0.35	24.20	24.27	0.20	23.47
		deVauc	23.24	24.58	23.62	2.42	0.52	45.91	0.34	24.20	23.64	0.16	22.68
		3.77	23.25	24.67	23.60	2.67	0.53	45.88	0.34	24.20	23.62	0.16	22.64
41310	40	disk	23.31	23.95	24.19	0.80	0.52	47.72	0.39	24.07	24.20	0.16	22.93
		deVauc	23.25	24.94	23.51	3.73	0.55	48.67	0.39	24.07	23.53	0.11	21.71
		4.60	23.23	24.96	23.48	3.90	0.53	48.65	0.39	24.07	23.50	0.11	21.70
52963	50	disk	22.91	24.19	23.32	2.22	0.43	4.20	0.55	23.29	23.34	0.20	22.38
		deVauc	22.78	25.05	22.93	7.04	0.38	5.80	0.53	23.29	22.97	0.16	21.74
		1.75	22.81	24.33	23.12	3.04	0.37	5.56	0.51	23.29	23.14	0.11	20.91
36361	94	disk	23.39	25.28	23.60	4.69	0.57	9.59	0.33	24.91	24.44	0.25	23.96
mask		deVauc	23.14	26.44	23.17	> 10	0.59	14.02	0.34	24.91	24.10	0.25	24.08
		0.51	23.42	24.87	23.76	2.77	0.56	7.22	0.33	24.91	24.59	0.25	23.92
47615	46	disk	22.11	22.51	23.42	0.43	0.84	80.08	0.56	23.57	23.44	0.25	23.06
		deVauc	22.07	22.77	22.88	0.90	0.80	78.31	0.57	23.57	22.91	0.20	22.57
		1.59	22.10	22.57	23.26	0.52	0.83	79.25	0.56	23.57	23.25	0.20	22.63
50415	85	disk	22.96	23.45	24.08	0.55	0.99	87.91	0.30	24.62	24.89	0.38	25.47
mask		deVauc	22.83	23.53	23.64	0.90	0.93	6.87	0.31	24.62	24.60	0.38	25.68
		0.75	22.96	23.42	24.12	0.52	0.88	57.55	0.30	24.62	24.92	0.34	25.15
50415	51	disk	22.84	23.40	23.83	0.67	0.92	72.84	0.35	23.74	23.84	0.38	24.44
mask		deVauc	22.68	23.52	23.36	1.15	0.89	52.31	0.35	23.74	23.52	0.34	24.35
		0.90	22.85	23.39	23.87	0.64	0.91	58.94	0.34	23.74	23.88	0.38	24.43
44126	42	disk	23.07	23.16	25.85	0.08	0.56	36.55	0.42	25.73	24.96	0.11	23.10
		deVauc	23.08	23.24	25.28	0.15	0.20	21.78	0.42	25.73	25.37	0.16	23.38
		0.02	23.05	23.12	26.19	0.05	0.67	65.22	0.42	25.73	25.25	0.11	23.55
42601	42	disk	21.35	22.86	21.67	2.99	0.73	23.95	0.82	21.69	21.73	0.65	23.43
		deVauc	20.83	23.25	20.96	8.24	0.73	25.99	0.85	21.69	21.59	0.65	23.62
		1.69	21.23	22.96	21.48	3.90	0.73	25.22	0.78	21.69	21.66	0.65	23.52
48284	85	disk	19.39	19.50	22.03	0.09	0.89	72.63	2.71	22.43	21.96	0.38	23.42
		deVauc	19.36	19.53	21.48	0.16	0.84	75.80	2.68	22.43	22.38	0.29	22.89
		4.27	19.35	19.52	21.47	0.16	0.94	62.78	2.68	22.43	22.45	0.34	23.25
39432	89	disk	22.28	22.46	24.38	0.17	0.92	45.11	0.33	24.92	25.18	0.25	24.83
		deVauc	22.19	22.44	23.95	0.24	0.86	57.15	0.33	24.92	24.82	0.25	24.95
		1.27	22.25	22.43	24.35	0.17	0.87	56.49	0.33	24.92	25.15	0.25	24.88
31898	30	disk	23.15	23.47	24.66	0.33	0.58	13.64	0.32	24.53	24.64	0.34	24.95
		deVauc	23.08	23.57	24.18	0.57	0.58	14.08	0.32	24.53	24.30	0.29	24.73
		1.71	23.13	23.50	24.49	0.40	0.58	14.16	0.32	24.53	24.51	0.34	25.00
15731	18	disk	19.81	19.90	22.67	0.07	0.94	87.59	3.27	22.99	21.84	0.11	20.42
mask		deVauc	19.74	19.89	21.97	0.14	0.88	3.49	3.29	22.99	21.88	0.16	21.59
		0.82	19.82	19.90	22.74	0.07	0.92	85.02	3.27	22.99	21.85	0.11	20.43
50997	85	disk	20.66	20.69	24.81	0.02	0.82	13.19	0.77	50	25.71	0.29	25.60
mask		deVauc	20.62	20.63	34.61	< 0.01	0.11	54.96	0.73	50	28.22	0.16	25.77
		10.00	20.52	20.53	50.00	< 0.01	0.10	35.78	0.73	50	25.41	0.07	21.96
50997	51	disk	20.43	20.46	24.41	0.02	0.67	10.88	0.63	24.49	25.04	0.43	25.30
mask		deVauc	20.42	20.47	23.94	0.04	0.54	1.20	0.64	24.49	24.38	0.34	24.83
		0.70	20.43	20.46	24.52	0.02	0.69	14.08	0.63	24.49	25.01	0.38	24.99
49298	52	disk	19.87	20.01	22.21	0.13	0.53	80.46	2.08	21.81	22.30	0.70	23.96
		deVauc	19.76	20.01	21.52	0.24	0.56	81.40	2.16	21.81	22.19	0.70	24.18
		0.79	19.87	20.00	22.29	0.12	0.52	80.74	2.08	21.81	22.44	0.79	24.13
49298	85	disk	19.92	20.03	22.48	0.10	0.41	32.97	1.50	23.63	23.50	0.79	25.48
		deVauc	19.77	20.05	21.42	0.28	0.36	36.29	1.52	23.63	23.34	0.79	25.55
		0.32	19.92	20.00	22.80	0.07	0.41	29.88	1.49	23.63	22.83	0.25	23.79
43151	95	disk	22.30	22.32	26.95	0.01	0.89	81.11	0.38	29.82	27.15	0.43	28.58
		deVauc	22.25	22.26	35.99	< 0.01	0.10	46.05	0.37	29.82	29.89	0.07	26.45
		7.66	22.21	22.22	36.23	< 0.01	0.10	39.37	0.37	29.82	50	0	0
43151	45	disk	22.37	22.42	25.94	0.03	0.88	51.65	0.39	28.83	25.96	0.43	26.78
		deVauc	22.36	22.41	25.89	0.04	0.37	69.94	0.39	28.83	26.15	0.38	27.18
		0.06	22.51	22.54	26.66	0.02	0.59	71.96	0.45	28.83	26.74	0.43	26.96

We include for each object: (1) its COMBO-17 ID; (2) the GEMS tile of the analyzed image (GOODS tile when larger than 78); (3) the fitted model, indicated as *disk* for a exponential profile, *deVauc* for a Vaucouleurs profile and index *N* for a Sersic profile, where this index shows the best fitted Sersic index; (4,5,6) the total, nuclear and host magnitude from the fitting; (7) the host-to-nucleus flux ratio; (8) the semiaxis ratio; (9) the position angle; (10) the fit reduced  $\chi^2$ ; (11) the peak subtracted magnitude (not model dependent); (12) the integrated magnitude over the restored host image; (13) the half-light radius, in arcsec and (14) the surface brightness at this radius, in mag arcsec<sup>-2</sup>. If an object image has been masked prior to fit we have indicated it with a *mask* in column (1).

butions of Fig. 4. For 3 of the remaining 4 objects, the classification was clear-cut in one band, and ambiguous in the other band (COMBO-17 36361 and 49298 in F606W, COMBO-17 50415 in F850LP). In these cases we adopted the morphological classification from that band where the type was found to be unambiguous. Only for one remaining object we

could not converge on a unique classification based on the fits alone. This object (COMBO-17 15731) has a Sersic index of 0.82 in F606W, indicative of a disk, and of 1.83 in F850LP, indicative of a spheroid. After visual inspection of images and surface brightness profiles we concluded that this object is most likely an early-type, bulge-dominated galaxy (especially

TABLE 3  
RESULTS FROM THE 2D FITTING: F850LP-BAND IMAGES

QSO ID	Tile	Model	Tot	Nuc	Host	H:N	a/b	P.A.	$z$	Sub	Emp	$r_{1=2}$	$r_{1=2}$
34357	94	disk	18.34	18.66	19.86	0.33	0.87	7.81	0.59	19.84	19.96	0.52	21.17
		deVauc	18.32	18.81	19.44	0.55	0.88	5.38	0.57	19.84	19.66	0.43	20.93
		3.33	18.34	18.82	19.48	0.54	0.86	4.63	0.58	19.84	19.64	0.38	20.64
41310	47	disk	22.56	23.29	23.35	0.94	0.41	39.73	0.31	23.30	23.35	0.25	22.99
		deVauc	22.53	24.12	22.82	3.31	0.99	4.57	0.32	23.30	22.82	0.20	22.45
		1.57	22.56	23.48	23.18	1.31	0.42	40.08	0.31	23.30	23.17	0.25	22.94
41310	40	disk	22.53	23.37	23.22	1.14	0.40	43.08	0.37	22.40	23.20	0.25	22.86
		deVauc	22.44	24.26	22.67	4.32	0.42	42.29	0.37	22.40	22.68	0.20	22.28
		2.92	22.49	24.18	22.75	3.73	0.44	42.50	0.37	22.40	22.75	0.20	22.27
52963	50	disk	22.23	23.41	22.68	1.95	0.56	2.14	0.36	22.72	22.66	0.25	22.21
		deVauc	22.10	24.20	22.27	5.91	0.47	5.31	0.35	22.72	22.28	0.20	21.71
		3.00	22.14	25.63	22.19	> 10	0.55	4.73	0.35	22.72	22.19	0.20	21.63
36361	94	disk	22.64	25.21	22.75	9.63	0.56	6.03	0.43	23.28	22.85	0.25	22.37
mask		deVauc	22.32	50.00	22.33	> 10	0.55	8.61	0.45	23.28	22.50	0.25	22.42
		0.95	22.64	25.10	22.76	8.62	0.56	5.93	0.43	23.28	22.87	0.25	22.38
47615	46	disk	21.41	22.64	21.84	2.08	0.88	87.85	0.47	21.96	21.82	0.30	21.81
		deVauc	21.27	23.80	21.39	9.20	0.89	84.30	0.49	21.96	21.42	0.25	21.52
		1.10	21.40	22.68	21.81	2.22	0.88	87.58	0.47	21.96	21.79	0.29	21.81
50415	85	disk	21.79	23.12	22.18	2.37	0.87	10.26	0.46	22.21	22.24	0.34	22.56
mask		deVauc	21.58	23.69	21.75	5.97	0.86	9.87	0.47	22.21	21.92	0.34	22.69
		1.09	21.79	23.15	22.16	2.48	0.87	10.21	0.46	22.21	22.23	0.34	22.57
50415	51	disk	21.79	23.02	22.22	2.08	0.89	71.82	0.33	22.23	22.21	0.34	22.53
mask		deVauc	21.59	23.66	21.77	5.70	0.88	74.96	0.34	22.23	21.85	0.34	22.63
		1.31	21.76	23.11	22.14	2.44	0.89	72.99	0.33	22.23	22.14	0.34	22.56
44126	42	disk	22.35	22.60	24.10	0.25	0.88	20.59	0.44	24.68	24.08	0.30	24.09
		deVauc	22.36	22.56	24.31	0.19	0.60	25.76	0.44	24.68	24.34	0.25	24.29
		0.16	22.36	22.50	24.67	0.13	0.69	49.28	0.43	24.68	24.66	0.29	24.16
42601	42	disk	20.32	22.28	20.52	5.05	0.77	24.14	0.47	20.46	20.53	0.56	21.94
		deVauc	19.90	23.40	19.95	> 10	0.78	23.41	0.44	20.46	20.32	0.56	22.09
		2.29	20.13	22.83	20.23	> 10	0.78	23.99	0.43	20.46	20.38	0.56	22.03
48284	85	disk	18.86	19.15	20.47	0.29	0.88	51.18	0.64	20.49	20.58	0.52	21.80
		deVauc	18.79	19.24	19.98	0.50	0.89	56.14	0.64	20.49	20.26	0.47	21.73
		3.31	18.89	19.31	20.15	0.46	0.95	6.09	0.71	20.49	20.30	0.38	21.30
39432	89	disk	21.41	21.87	22.57	0.52	0.94	9.41	0.40	22.59	22.69	0.30	22.66
		deVauc	21.32	21.93	22.26	0.73	0.90	19.89	0.41	22.59	22.40	0.29	22.88
		1.79	21.41	22.00	22.36	0.71	0.93	43.26	0.40	22.59	22.42	0.25	22.28
31898	30	disk	21.86	23.35	22.19	2.91	0.58	17.14	0.31	22.01	22.18	0.34	22.44
		deVauc	21.61	24.31	21.71	> 10	0.58	17.61	0.31	22.01	21.80	0.34	22.50
		2.52	21.72	23.93	21.88	6.60	0.58	17.45	0.30	22.01	21.91	0.34	22.48
15731	18	disk	19.50	20.02	20.56	0.60	0.99	78.40	0.77	20.66	20.74	0.56	22.04
mask		deVauc	19.30	20.11	20.00	1.10	0.91	24.68	0.77	20.66	20.39	0.47	21.83
		1.83	19.45	20.07	20.36	0.76	0.93	38.40	0.76	20.66	20.45	0.47	21.78
50997	85	disk	20.36	20.49	22.75	0.12	0.63	23.78	0.49	22.94	22.16	0.20	21.81
mask		deVauc	20.34	20.65	21.88	0.32	0.80	15.77	0.52	22.94	22.01	0.25	22.09
		0.83	20.36	20.58	22.22	0.22	0.79	13.44	0.52	22.94	22.27	0.29	22.22
50997	51	disk	20.29	20.40	22.84	0.10	0.63	40.80	0.39	22.77	22.85	0.29	22.85
mask		deVauc	20.27	20.46	22.29	0.18	0.61	44.89	0.39	22.77	21.83	0.16	20.88
		1.39	20.28	20.41	22.73	0.11	0.62	41.68	0.39	22.77	22.75	0.29	22.85
49298	52	disk	19.46	19.79	20.92	0.35	0.55	82.13	0.79	21.13	20.78	0.65	22.65
		deVauc	19.13	19.82	19.96	0.87	0.47	81.49	0.82	21.13	21.07	0.88	23.24
		0.95	19.46	19.79	20.94	0.34	0.55	82.22	0.79	21.13	20.78	0.65	22.64
49298	85	disk	19.50	19.83	20.99	0.34	0.50	28.65	0.72	21.10	20.86	0.56	22.61
		deVauc	19.24	19.86	20.15	0.76	0.45	30.25	0.75	21.10	21.09	0.75	23.23
		0.70	19.51	19.81	21.09	0.30	0.50	27.75	0.72	21.10	20.93	0.56	22.58
43151	95	disk	21.80	22.12	23.31	0.33	1.00	68.38	0.51	23.31	23.39	0.20	22.62
		deVauc	21.75	22.23	22.87	0.55	0.83	68.29	0.51	23.31	22.80	0.16	21.85
		0.87	21.80	22.10	23.36	0.31	0.83	71.44	0.51	23.31	23.11	0.20	22.51
43151	45	disk	21.93	22.22	23.52	0.30	0.98	82.06	0.39	23.72	23.55	0.29	23.52
		deVauc	21.91	22.37	23.07	0.52	0.89	79.39	0.39	23.72	23.08	0.25	23.20
		1.20	21.92	22.23	23.44	0.32	0.97	79.46	0.39	23.72	23.44	0.29	23.50

Columns as in table 2

in the redder F850LP band) without significant evidence of a disk, but with two faint blue arms sticking out in the F606W (rest-frame B band) residual images (see Fig. A10). These “arms” could also be tidal features resulting from interaction with the close companion of that galaxy, owing their blue colors to enhanced star formation. We also note that contrast between nucleus and host is considerably more favourable in the F850LP band for this  $z = 0.83$  AGN, giving additional weight to its classification as an early-type galaxy.

Based on the assigned type, we estimated the nuclear magnitude using the value derived from the 2D fitting. The host magnitude was measured from the actual data through a large circular aperture after removing the nucleus. The structural parameters  $r_{1=2}$  and  $r_{1=2}$  were obtained from the surface brightness analysis. Finally, we flagged each object with a value between 0 and 3 to describe its degree of interaction (based upon visual inspection), where 0 means no nearby companion within a projected radius of  $2''$  (i.e., 13 kpc at

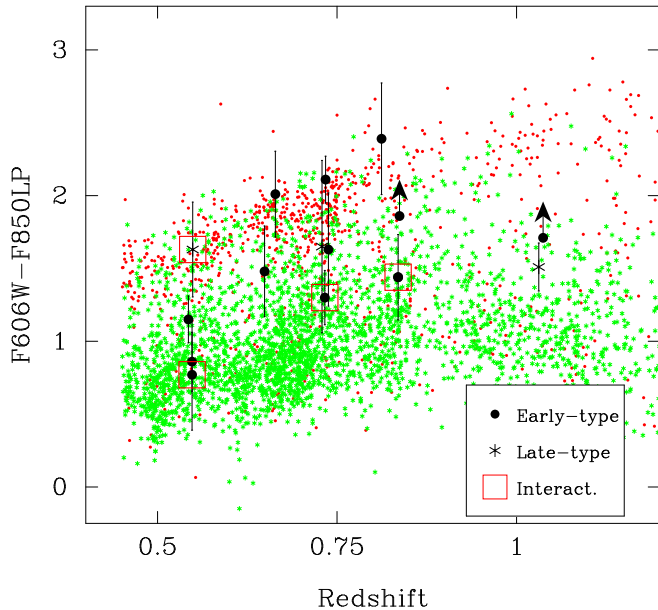


FIG. 5.— Observed  $F606W - F850LP$  colors for the host galaxies as a function of redshift (large symbols). The solid circles show morphologically early-type galaxies, the stars morphologically late-type galaxies (see text for details). The open squares mark the objects with evidence of interactions/mergers (class 2 and 3 in Table 4). The small symbols indicate early-type ( $n \geq 2.5$ , red solid circles) and late-type ( $n < 2.5$ , green stars) inactive galaxies observed in the GEMS field.

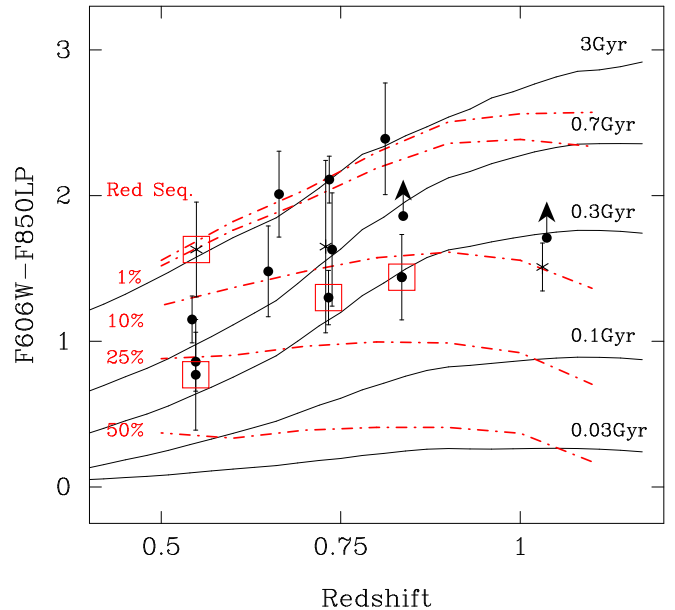


FIG. 6.— Observed  $F606W - F850LP$  colors for the host galaxies as a function of redshift (large symbols), compared to simple populations models. The symbols are the same as those in Fig. 5. The solid lines show the expected colors of a single stellar population with different ages. The dashed lines show the expected colors of a mixed population, with a dominant old stellar population and a varying contribution of light from young stellar populations, derived completely empirically (see Section 5.1 for details).

the mean redshift of our sample); 1 means at least one nearby companion, but no tidal tails or bridges between the host and the companion; 2 indicates a nearby companion with an apparent bridge between the host and the companion, and 3 signifies objects clearly undergoing a merger event. Table 4 lists the final estimated parameters for our objects, separately for the  $F606W$  and  $F850LP$ -band images, including the morphological classification and the interaction level flag. The listed magnitudes have not been corrected for Galactic extinction, which is however small. For the values quoted hereafter, we adopt a Galactic extinction of  $E(B - V) = 0.008$  mag, which corresponds to corrections of 0.024 and 0.014 mag for the  $F606W$  and  $F850LP$  bands, respectively (Schlegel et al. 1998). In the Appendix we present color images and surface brightness profile of the original data, the model, the restored host galaxy and the residuals, together with notes on individual objects.

We find that 3 of the 15 objects show evidence of a major merger: COMBO-17 52963, COMBO-17 36361 and COMBO-17 42601. The images of these objects show generally blue clumpy structures, with linear shapes, as expected from star forming regions induced by recent merger events. In some cases it is difficult to distinguish these structures from those expected from spiral arms (e.g., COMBO-17 42601), although the lack of disk-structure in the profile suggests a merger process. Another object, COMBO-17 15731 shows a companion with what seems to be a bridge connecting it with the host. Finally, two other objects show what could be close companions, without any evidence of connection between them and the hosts. Therefore, a fraction between 20% and 40% of the objects shows some degree of interaction with close companions, from major merger to low-level interaction.

Twelve of the 15 hosts – 80% of the sample – are morpho-

logically early-type galaxies, as defined by the Sèrsic index. This fraction is not affected if we exclude the 3 possibly merging galaxies. On the other hand, only one object can be clearly classified as a disk-dominated galaxy (COMBO-17 49298). Two other galaxies could also have significant disks, of which COMBO-17 36361 is heavily distorted, and the classification is uncertain.

## 5. DISCUSSION

### 5.1. The colors of the host galaxies

The average observed color of all the hosts is  $F606W - F850LP = 1.55 \pm 0.45$  mag, without significant differences between morphological classes ( $1.54 \pm 0.48$  for the early-type hosts and  $1.65 \pm 0.09$  for the late-type hosts, excluding mergers and strongly interacting systems). We have compared the host and nuclear colors in order to check if there were a possible contamination from the nucleus, due to improper subtraction, that could affect our results. No significant trend is seen between the nuclear and host colors.

Figure 5 shows the  $F606W - F850LP$  distribution of the host galaxies as a function of redshift. For comparison, we included the same distribution for the 4000 inactive galaxies in the GEMS field at the redshift range of our objects. A detailed study of these objects will be presented in forthcoming papers by the GEMS collaboration (Barden et al., in prep.; Wolf et al., in prep.; McIntosh et al., in prep.). The red sequence of early-type galaxies, as discussed by Bell et al. (2004), is clearly identified in the figure as a red envelope, and shows the color of the oldest stellar populations at a give epoch. It is clear from Fig. 5 that the host galaxies, despite their morphological types, range in their colors from the red sequence to blue colors indicative of ongoing or recent star formation. In particular, the morphologically early-type hosts tend to be bluer, on average, than the red sequence galaxies,



TABLE 4  
SUMMARY OF THE RESULTS OF OUR ANALYSIS

QSO ID	z	Class	F606W <sub>QSO</sub>	F606W <sub>Nuc</sub>	F606W <sub>host</sub>	r <sub>1=2</sub>		1=2		Morph.	Inter.			
34357	0.543	deVauc	19.19	0.02	19.53	0.03	20.82	0.05	2.73	0.72	21.4	0.2	Early Type	0
41310	0.548	deVauc	23.24	0.04	24.58	0.06	23.55	0.26	0.74	0.23	20.3	0.2	Early Type	1
52963	0.548	deVauc	22.78	0.03	25.05	0.07	22.97	0.22	0.68	0.21	19.4	0.2	Early Type	3
36361	0.549	disk	23.39	0.02	25.28	0.07	24.24	0.14	1.32	0.42	22.1	0.2	Late Type	3
47615	0.649	deVauc	22.07	0.03	22.77	0.03	22.91	0.17	1.12	0.34	20.4	0.2	Early Type	0
50415	0.664	deVauc	22.96	0.03	23.45	0.03	24.00	0.14	2.13	0.61	22.2	0.2	Early Type	1
44126	0.729	disk	23.07	0.04	23.16	0.06	24.46	0.52	0.63	0.17	20.7	0.2	Late Type	0
42601	0.733	deVauc	20.83	0.02	23.25	0.05	21.59	0.06	3.75	1.15	21.2	0.3	Early Type	3
48284	0.734	deVauc	19.36	0.02	19.53	0.03	22.38	0.05	1.85	0.58	20.7	0.2	Early Type	0
39432	0.738	deVauc	22.19	0.02	22.44	0.03	24.73	0.26	1.44	0.46	21.7	0.3	Early Type	0
31898	0.812	deVauc	23.08	0.04	23.57	0.06	24.20	0.26	1.89	0.59	22.3	0.3	Early Type	0
15731	0.835	disk	19.81	0.02	19.90	0.03	21.84	0.17	0.65	0.18	17.8	0.1	Early Type	2
50997	0.837	Not Det.	20.62	0.02	20.63	0.03	—	—	—	—	—	—	Early Type	1
49298	1.031	disk	19.87	0.02	20.01	0.03	22.30	0.05	4.27	1.28	21.9	0.2	Late Type	0
43151	1.037	Not Det.	22.30	0.02	22.32	0.03	—	—	—	—	—	—	Early Type	0

QSO ID	z	Class	F850LP <sub>QSO</sub>	F850LP <sub>Nuc</sub>	F850LP <sub>host</sub>	r <sub>1=2</sub>		1=2				
34357	0.543	deVauc	18.32	0.02	18.81	0.05	19.66	0.06	2.15	0.63	18.9	0.2
41310	0.548	deVauc	22.53	0.05	24.02	0.16	22.67	0.37	1.16	0.35	20.6	0.3
52963	0.548	deVauc	22.10	0.04	24.10	0.16	22.19	0.37	1.05	0.32	19.8	0.3
36361	0.549	disk	22.64	0.05	25.13	0.19	22.60	0.38	1.32	0.42	20.5	0.3
47615	0.649	deVauc	21.27	0.04	23.71	0.15	21.42	0.22	1.51	0.45	19.5	0.3
50415	0.664	deVauc	21.58	0.04	23.60	0.15	21.79	0.26	1.91	0.56	20.4	0.3
44126	0.729	disk	22.35	0.04	22.60	0.07	22.80	0.60	1.67	0.52	21.7	0.5
42601	0.733	deVauc	19.90	0.02	23.40	0.13	20.28	0.14	3.23	0.98	19.7	0.3
48284	0.734	deVauc	18.79	0.02	19.24	0.05	20.26	0.06	2.48	0.75	19.1	0.3
39432	0.738	deVauc	21.32	0.04	21.82	0.14	22.30	0.29	1.56	0.46	20.2	0.3
31898	0.812	deVauc	21.61	0.04	24.21	0.16	21.80	0.26	2.00	0.59	19.9	0.3
15731	0.835	deVauc	19.30	0.02	20.11	0.05	20.39	0.06	2.79	0.82	19.2	0.3
50997	0.837	deVauc	20.34	0.02	20.65	0.05	21.92	0.26	1.36	0.40	19.3	0.3
49298	1.031	disk	19.46	0.02	19.79	0.05	20.78	0.09	3.97	1.22	19.6	0.2
43151	1.037	deVauc	21.75	0.04	22.12	0.14	22.65	0.36	1.65	0.46	20.3	0.3

We include for each object and band the COMBO-17 id. (1), the redshift (2), the host classification (italics when dubious) (3), the total magnitude (4), the nucleus and host magnitudes (5,6), the host structural parameters, the half-light radius in kpc (7) and the surface brightness at this radius, corrected for cosmological dimming (8), the final morphological classification (italics when dubious) (9) and a flag indicating the interaction degree (10). The interaction degree has been visually classified as: 0 Isolated galaxies, 1 Galaxies with a close companion, 2 Galaxies with tidal tails and bridges with a close companion and 3 clear mergers. The listed magnitudes have not been corrected for galactic extinction.

hinting at the presence of significant younger stellar population. Roughly 50–70% of the 10 early-type hosts detected in both bands are bluer than the red sequence galaxies.

There are several combinations of stellar populations that could explain the observed distribution. We discuss two extreme cases: (a) The galaxy has a single stellar population, formed in a single burst of star formation; and (b) the galaxy is dominated by an old stellar population, similar to the stellar population of field early-type galaxies, but it has undergone recent star formation. Figure 6 shows schematically the same color distribution as Fig. 5, but now we overplotted the expected colors for the two scenarios. Solid lines show the colors of single stellar populations. These colors were calculated using the Bruzual & Charlot (2003) models, assuming a solar metallicity and a Chabrier (2003) IMF (we also tried a Salpeter (1955) IMF, without significant differences). These isochrones are a rough indicator of the luminosity-weighted age of the host galaxies. A wide range of ages, from ~0.3 Gyr to ~3 Gyr, is required to explain the observed distribution. In average they seem to have moderately young luminosity-weighted stellar populations, with an age of ~1 Gyr. These ages are indicators of the wide range of stellar populations needed to describe the colors of the host galaxies in our sample.

Yet, a mix of different populations can also generate similar colors. The dashed lines in Figure 6 show the colors of GEMS red sequence galaxies (taken to empirically represent an old stellar population), where a varying fraction of

young stellar population has been added to the overall mass. The young stellar population has been characterized by the population of the galaxies in the blue end of the U–V color-diagram distribution for the GEMS field ( $U - V < 0$  mag). This model-independent approach has been cross-checked substituting this young population with a 0.03 Gyr model without appreciable changes. It is seen that the colors of the host galaxies can be reproduced by adding a varying mass fraction between close to 0% and ~30% of young stars to an overall population of old stars.

It is worth noting that uncertainties from dust reddening and metallicity only mildly affect our conclusion that substantial young stellar populations are present in many of the AGN host galaxies. In particular, dust tends to dim and redden young stars preferentially (e.g. Calzetti et al. 1994; Zaritsky 1999), which, if corrected for, would imply even larger young stellar population fractions in our hosts. On the other hand, changes in metallicity by a factor 3, in the sense that hosts would have lower metallicity, could reproduce the color offsets seen between the early-type inactive and active galaxies. However, recalling the typically high luminosities of the AGN host galaxies, coupled with the metallicity–luminosity correlation and inspecting the spatial clumping of the blue stars in many of the recovered host galaxy images (Fig. A10), it seems rather unlikely that a metallicity difference between active and non-active morphologically early-type galaxies could be the dominant factor in driving the observed color differences. Moreover, it is well known that QSO broad-line re-

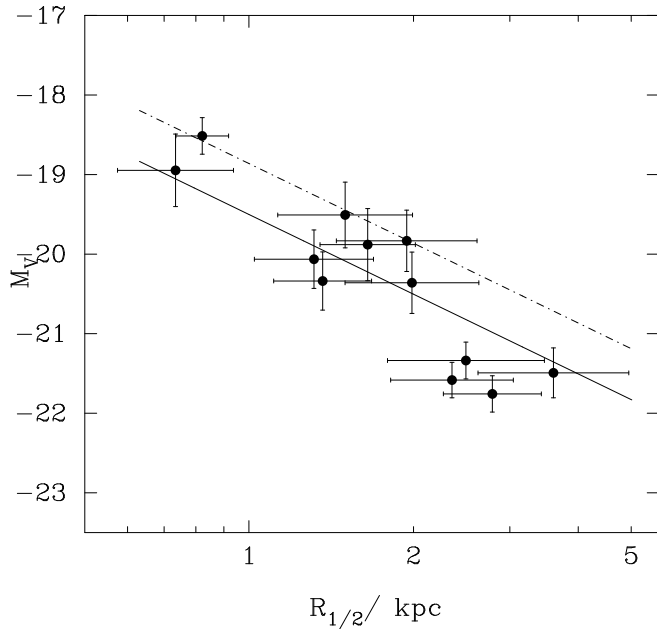


FIG. 7.— Plot of the host galaxy absolute magnitude against half-light radius for the 12 early-type galaxies of our sample (solid circles). The solid line shows the location of the luminosity-size relation for early-type red sequence galaxies at the mean redshift of our objects (Schade et al. 1997). The dashed-dotted line shows the relation at  $z = 0$  (Kormendy 1977).

gions have high metallicities (Hamann & Ferland 1992, 1993; Constantin et al. 2002). There is thus no evidence for low metallicities in the host galaxies as an explanation for the blue colors.

### 5.2. Absolute magnitudes, scale-lengths and stellar masses of the host

We calculated  $k$ -corrections for the host galaxies to obtain rest-frame  $U-V$  colors and absolute magnitudes that allowed us to compare them with the inactive galaxies in the GEMS field. In the Appendix (Section B), we describe in detail the method adopted to derive those transformations. We used the observed F606W–F850LP colors to derive the rest-frame  $U-V$  colors, using these transformations, including the standard deviation of each transformation in the color errors. Recall that for the redshift range of the sample, these bandpass shifts from F606W–F850LP to  $U-V$  and therefore the color transformations are relative small. Once determined the rest-frame  $U-V$  colors, we derived the absolute magnitudes of our objects, using the transformations described in the Appendix, including the standard deviation of each transformation in the magnitude errors. The mean  $V$ -band absolute magnitudes of our AGN host galaxies is  $M_{V, \text{host}} = -20.2 \pm 1.2$  mag, covering a range between  $-18.5$  and  $-22$  mag.

We determined the half-light radii of these galaxies from the scale lengths obtained in the fits, computing a luminosity weighted average of the values obtained for both bands (Table 4). The average half-light radius is  $r_{1/2} = 1.9 \pm 0.3$  kpc. Figure 7 shows the distribution of the absolute magnitudes as function of these radii. For comparison, we overplot the luminosity-size relation of early-type galaxies at the average redshift of our sample (Kormendy 1977; Faber et al. 1987). We adopted the luminosity-size relation obtained by Schade et al. (1997) for red sequence early-type galaxies in clusters at  $z = 0.7$ , transformed to our cosmology. The loci of

the early-type active and inactive galaxies in the luminosity-size plane are consistent with each other.

We estimated the stellar masses using the average relation found by Bell & de Jong (2001) between the  $M = L$  and the  $B-V$  color. For that we have estimated the  $B-V$  colors of our objects using the relation between the  $U-V$  and the  $B-V$  colors derived from the field galaxies in the COMBO-17. The correlation between both colors is tight, with a dispersion of  $0.07$  mag. Using these colors and the  $V$ -band absolute magnitudes of our objects we have an estimate of the stellar masses of our host galaxies. The average mass derived for the early-type hosts is  $1.5 \times 10^{10} M_{\odot}$ , with a range of masses between  $0.1$  and  $5.9 \times 10^{10} M_{\odot}$ . We find AGN harboured by early-type galaxies with a wide range of masses, not restricted to the most massive ellipticals, as previously reported by the studies of more luminous QSO hosts (e.g. Dunlop et al. 2003).

### 5.3. The $U-V$ color-magnitude diagram

Figure 8 shows the  $U-V$  vs.  $M_V$  color-magnitude diagram for the hosts, together with these values for  $\sim 4000$  inactive galaxies from the GEMS sample at the same redshift of our objects. For consistency we have used the same grid of transformations (described above) for deriving the rest-frame colors and absolute magnitudes of the active and inactive galaxies, using the observed F606W and F850LP magnitudes. The morphological early- and late-type galaxies, as classified within the GEMS project (Barden et al., in prep.; Bell et al. 2004), have been indicated with red solid circles and green stars, respectively. The red sequence of early-type galaxies, described by Bell et al. (2004) for the GEMS inactive galaxies at  $z = 0.7$ , is clearly visible in Fig. 8. From this figure, we can see that between  $5-7$  of the morphological early-type hosts are bluer than the red sequence early-type galaxies ( $\sim 50-70\%$  of the sample). The range depends on where we draw the line for including objects in the red sequence ( $U-V = 0.6-0.8$ ). On the other hand, only  $\sim 30\%$  of the host galaxies detected in both bands are clearly as red as red sequence galaxies. This fraction would increase to  $\sim 40\%$  if we included the two hosts not detected in the F606W-band.

We performed 1D and 2D Kolmogorov-Smirnov tests on the color and color-magnitude distributions of the early-type host galaxies and the early-type inactive red sequence galaxies. The null hypothesis that both samples were drawn from the same parent population has probabilities of only  $0.1$  and  $0.4\%$ , respectively. The standard KS tests do not take the errors into account. To determine the extend to which these errors can affect our results we simulated 1000 color and color-magnitude distributions. We add random values to the original colors and magnitudes following Gaussian distributions with the width of the errors. Repeating the KS tests on these simulated distributions we find that the acceptance probabilities of the null hypothesis are only marginally larger, with  $0.8$  and  $0.5\%$ , respectively. We conclude that the distribution of early-type AGN host galaxies is significantly different than that of the red sequence.

However, as previously reported by Bell et al. (2004) there is a tail of blue, but morphologically early-type galaxies which is clearly seen in Fig. 8. Using a similar KS test, we find the color and color-magnitude distributions of the early-type host galaxies are actually consistent with being drawn from the *complete* sample of inactive early-type galaxies, i.e. including the blue tail. The probabilities found by a KS test on both samples are  $16.7\%$  ( $21.7\%$ ) and  $39.1\%$  ( $34.1\%$ ),

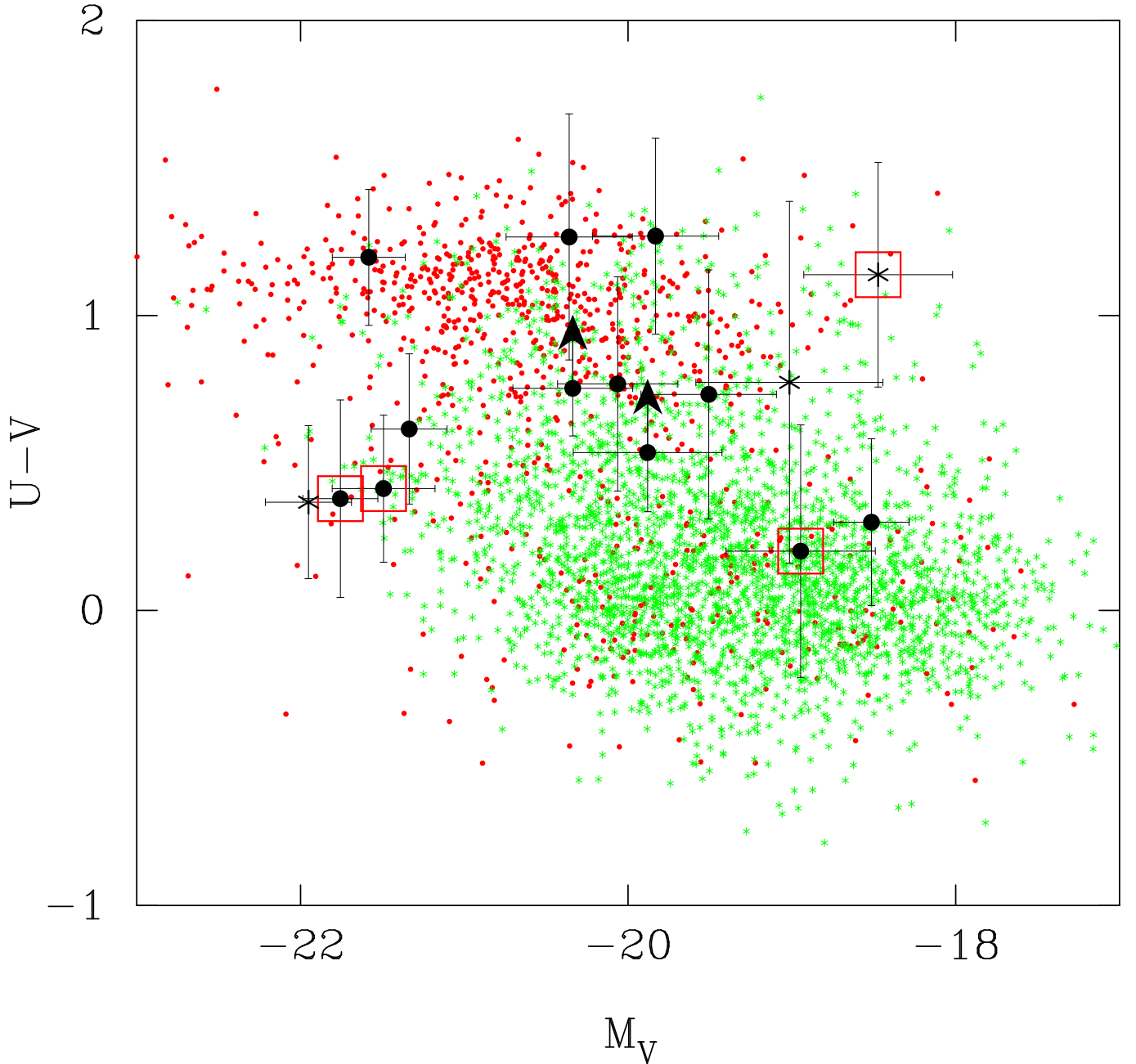


FIG. 8.— Rest-frame color-magnitude distribution of the host galaxies of active nuclei compared with the inactive galaxies from GEMS from the same redshift range as our AGNs (symbols as in Fig. 5). The red sequence for early types is clearly identified in the field galaxy distribution (at  $U - V \approx 0.8$ ). The hosts, mainly early-type galaxies, are bluer than the red-sequence galaxies in the field. There is a clear cutoff in the upper-right corner due to combined effect of the different detection limits in the F606W and the F850LP bands. This limit does not affect our results.

for the color and color-magnitude distributions without and with the inclusion of errors, respectively. However, applying a luminosity cut at  $M_V < -21$ , which isolates the four most luminous early-type host galaxies, the color distributions are again markedly different, although due to the reduce number of objects a KS test would not produce a reliable probability. These objects harbor the four most luminous AGNs of our sample.

In summary, we have found that the host galaxies of AGNs are mainly elliptical galaxies ( $\sim 80\%$ ), with  $20-40\%$  showing evidence of interactions. Only  $\sim 20\%$  are disk dominated. Roughly  $50-70\%$  of the host galaxies that are struc-

turally early-type are bluer than the red sequence early-type galaxies, indicating the presence of younger stellar populations than that of the inactive early-type galaxies. Taking into account the recently reported blue tail for early-type galaxies (Bell et al. 2004), their colors become more similar, but they still remain significantly bluer for the most luminous objects. However, they are structurally similar to red sequence early-type galaxies, which may indicate that they are dominated by an underlying old stellar population with only a small fraction of the mass involved in a recent star formation episode.

#### 5.4. Comparison with recent results

The majority of previous studies of host galaxies was focused on host morphologies (e.g. Dunlop et al. 2003; Sánchez & González-Serrano 2003). They found that the QSO hosts were mainly early-type galaxies, with an increase of the fraction of early-type galaxies with nuclear luminosity (Dunlop et al. 2003). The fraction of late-type host galaxies ranges between 15 and 35 % for radio-quiet QSOs, and almost zero for radio-loud QSOs (Dunlop et al. 2003; Floyd et al. 2003; Sánchez & González-Serrano 2003; Hamilton et al. 2002). These fractions are similar to those found in our sample ( $\sim 20\%$ ), and there is no significant change with redshift. In contrast, very few studies have focused on colors. Kauffmann et al. (2003) have recently presented their results based in the comparison of active and inactive galaxies from the SDSS survey at  $0.02 < z < 0.3$ . They found that the host galaxies of both type 1 and 2 AGNs have younger mean stellar ages than inactive galaxies, possibly due to starburst or post-starburst populations. Furthermore, 40 % of their objects are blue *pure* spheroids, and they found evidence of recent interactions in  $\sim 30\%$  of their objects. Their subsample of type 1 AGNs covers a similar range of luminosities compared to our sample. Jahnke et al. (2004) already noticed that the mean colors of the hosts of their complete sample of low- $z$  type 1 AGNs were bluer than expected, especially for pure elliptical galaxies. Similar results have been found by Kotilainen & Falomo (2004), for a sample of low- $z$  BL Lac host galaxies. Their results are remarkably similar to the ones presented here, especially regarding the existence of a population of blue elliptical hosts. Our results extend this result to early epochs, covering the last half of the cosmic history.

On the other hand, Dunlop et al. (2003) did not find especially blue colors for their sample of low- $z$  high luminosity QSO hosts, based on the analysis of  $R$  and  $K$ -band images (Dunlop et al. 1993; McLure et al. 1999). However, the fraction of young stars required to reproduce our observed colors would not produce significant deviations in  $R - K$  color at low- $z$  because the red light from blue stars is small compared to the light from the dominant underlying stellar populations. Furthermore, Nolan et al. (2001) show evidence for a small fraction of young stellar population in their spectroscopic analysis of the host galaxies studied by Dunlop et al. (2003).

In a companion article (Jahnke et al. 2004), we have analyzed the host galaxies of AGNs in the GEMS project at high- $z$  ( $1.3 < z < 2.5$ ). We found evidence for significant UV flux from young stars in all the detected host galaxies, in a clear agreement with current results.

It seems that the basic ingredients in generating a powerful AGN are a massive black hole *and* an abundant fuel supply, as already expressed by Kauffmann et al. (2003). Only massive early-type galaxies contain massive black holes, and only galaxies with significant amounts of recent star formation have the required fuel supply. It is still an open question why these early-type galaxies retain enough gas to undergo star formation, and what is the relationship between the AGN and the star formation activity.

##### 5.5. AGN activity and star formation: why are our early-type hosts blue?

The correlation between nuclear activity and enhanced star formation could arise from an enrichment of gas due to recent merger events. The merger would produce the infall of gas needed to (re)ignite the AGN and trigger star formation

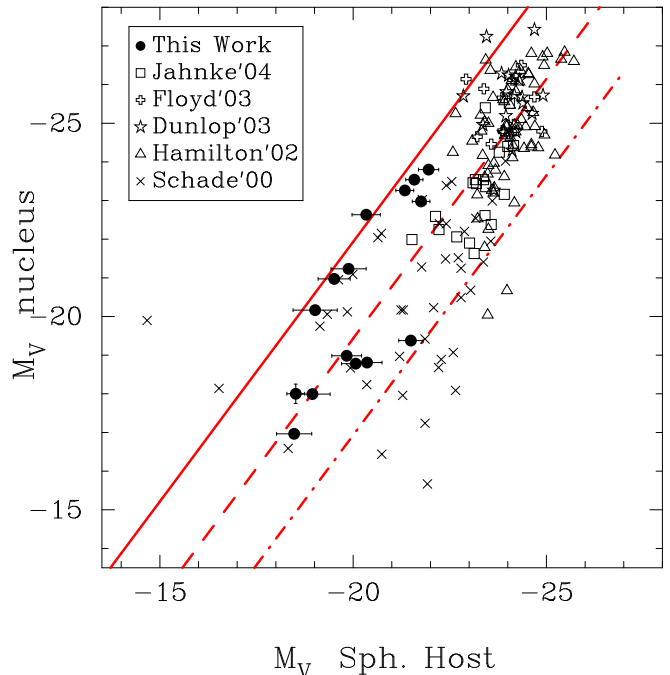


FIG. 9.— Distribution of the F606W-band absolute magnitudes of nucleus along the F606W-band absolute magnitude of the spheroidal host galaxies of our sample (solid circles), together with different samples taken from the literature. The solid, dashed and dot-dashed lines show the expected location for an AGN emitting at 100 %, 10 % and 1 % of the Eddington limit, respectively.

at the same time (e.g., Lin et al. 1988; Mihos & Hernquist 1996; Corbin 2000). We find evidence of recent mergers in  $\sim 20\%$  of our sample, a fraction similar to the values reported in the literature (e.g., Kauffmann et al. 2003; Sánchez & González-Serrano 2003). However, it is not clear that this fraction could be considered as a significant excess of merging galaxies. The fraction of merging galaxies in the local universe is rather small,  $\sim 7\%$ , based on classical studies like Shapley & Ames (1932). But this fraction is known to increase with the redshift. For example, van den Bergh et al. (1996) and Lee & Hwang (2000) found that at least  $\sim 39\%$  of the galaxies in the HDF-N and HDF-S show disrupted morphologies, reminiscent of mergers. Therefore, if a merger is the cause of the enrichment of gas in these galaxies, this event must have happened long before the morphological relaxation of the galaxy, in the majority of the cases.

Galaxy interactions have been claimed for decades to be important triggers of star formation (Larson & Tinsley 1978; Kennicutt et al. 1987, e.g.). It was also believed that mergers produce an enrichment of gas, and even minor interactions can trigger star formation due to the infall of gas, compression and heating (e.g. Barton et al. 2000). In particular, tidal interaction can trigger star formation that significantly affects the colors of the nuclear region (e.g. Barton et al. 2003). (But see Bergvall et al. 2003, for a counter example). This may well be the kind of effect we detect in our observations, where we can reproduce the observed colors with a small fraction of young stars. Mihos & Hernquist (1996) estimated the timescales of star formation induced by interaction to be  $\sim 10 - 100$  Myr, which is of the same order as the morphological relaxation time of  $\sim 50 - 100$  Myr (depending on the scale length of the galaxies involved). Since even a somewhat aged population of recently formed stars can still produce sub-

stantially blue colors in the host galaxy (see the model tracks in Fig. 6), we may well still see the enhanced blue color while the morphological signatures of the merger or interaction have disappeared.

Another possibility could be that the gas was already present in the morphological early-type parent galaxy. As stated above, there is a tail of blue elliptical galaxies in the color distribution of early-type galaxies in the GEMS sample – that is, morphological early-type galaxies with enough gas to undergo star formation. In that case a process such as a minor merger, which would hardly be detectable by our current morphological analysis, could produce the infall of this gas into the inner regions.

A completely different connection between AGN and star formation activity could come from AGN-driven feedback processes. The combined effect of the ionizing radiation and possible mechanical outflows trigger star formation throughout the host galaxy. The implications of AGN feedback for galaxy evolution in general are still poorly understood (e.g. Colbert et al. 1996; Silk & Rees 1998).

### 5.6. The host-nucleus luminosity relation

McLeod & Rieke (1994) found that a minimum host luminosity appears to be required to produce an AGN of given luminosity. This result has been confirmed by different authors (e.g., Dunlop et al. 2003; Floyd et al. 2003; Sánchez & González-Serrano 2003; Jahnke et al. 2004). Therefore, the upper envelope of the nuclear luminosities shows a correlation with host luminosities. The widely accepted interpretation is that for a given host luminosity, the mass of the central black hole is given by the bulge/BH mass correlation (Magorrian et al. 1998; Ferrarese & Merritt 2000; Häring & Rix 2004), and that each nuclear source has a maximum luminosity given by the Eddington limit. The spread in the nuclear-to-host luminosity ratio distribution would then be largely produced by different accretion rates, implying  $L = L_{\text{Edd}}$  to range from 0.01 to 1 (assuming a fixed radiative efficiency for all the objects).

Figure 9 shows the distribution of the nuclear absolute magnitudes versus the absolute magnitudes of the spheroidal hosts for our sample (solid circles), together with different samples of type 1 AGNs obtained from literature. We have taken the bulge luminosities whenever the bulge/disk components of the hosts have been decoupled (e.g. Schade et al. 2000). The Jahnke et al. (2004) sample has been included for a comparison with another complete sample of slightly brighter AGNs, at a lower redshift range,  $z < 0.2$  (open squares, 19 objects). We have included two well-defined samples of different families of even brighter AGNs (Dunlop et al. 2003; Floyd et al. 2003), that include radio-loud and radio-quiet quasars (open stars and open crosses, 19 and 14 objects respectively). The compilation by Hamilton et al. (2002) bundles a large collection of HST observations, but it is not, in any sense, a complete or well-defined sample (triangles, 70 objects). Finally we have included an X-ray selected sample of type 1 AGNs, from Schade et al. (2000). Despite the large dispersion, it is clear that all the samples follow the same trend.

In this figure we have overplotted the expected locations for AGN emitting at certain fractions of the Eddington limit, assuming a luminosity dependent bulge mass-to-light ratio, following Dunlop et al. (2003) and Floyd et al. (2003). Despite a few AGN that appear to show super-Eddington luminosities, the distribution of points is in agreement with a maximum of  $L = L_{\text{Edd}}$ . The mean distribution follows mainly the

expected location for an object emitting at 10 % of  $L_{\text{Edd}}$ , (dashed line), while 90 % of the objects are confined within a range of fuelling efficiencies between 100 % and 1 % of the Eddington limit (solid and dashed-dotted line). There is no evidence that the upper limit to the nuclear luminosity at given host luminosity could depend on either the host luminosity or redshift.

As discussed above, the mass-to-light ratio depends on the  $U - V$  color (e.g., Bell & de Jong 2001). At a given luminosity, blue galaxies are less massive than red ones. If host galaxy mass is translated into expected black hole mass, this implies that the Eddington limit for the nucleus of a blue host galaxy is lower than that for the nucleus of a red host galaxy with the same luminosity. The Eddington limit plotted in figure 9 corresponds to a red spheroidal, and therefore, is an upper limit. As we quoted in Section 5.1, the blue colors of the host galaxies are most probably produced by a recent star formation involving less than a 30% of the overall host mass. In that case the Eddington limit would be 0.3 mag fainter for the bluest host galaxies of our sample, which does not change the overall results.

## 6. SUMMARY AND CONCLUSIONS

We have analyzed a flux-limited sample of 15 intermediate luminosity type 1 AGNs from COMBO-17, at  $0.5 < z < 1.1$  using the GEMS deep F606W and F850LP-band ACS images. We decomposed the host and nuclear components and detected the host in all the F850LP-band images (and in 13 of the F606W-band images). A morphological analysis has been performed to determine if the hosts were bulge or disk-dominated objects. 80 % of the hosts are spheroidal galaxies, and only 1 object can be clearly classified as a disk dominated galaxy. We found evidence for on-going mergers in 25 % of the early types and 30 % of the late type hosts.

The host galaxies show a wide range of F606W – F850LP colors, indicating the presence of different stellar populations. We found that a large fraction of the early-type hosts, 50–70%, show distinct blue colors when comparing with the red sequence inactive early-type galaxies studied by GEMS at the same redshift range. The color and color-magnitude distributions of the AGN hosts are significantly different from those of red sequence galaxies. On the other hand, the absolute magnitudes, effective radii and stellar masses of these objects are remarkably similar to normal elliptical galaxies. Therefore, a significant fraction of the AGN in our sample seem to be located in *young spheroids*.

We considered two different simplified scenarios that can explain the observed color distributions: (a) a single stellar population with a mean age of close to 1 Gyr, or (b) a mix of an underlying old stellar population plus a small mass fraction in a young component. Both can describe the observed colors well. On the other hand, the early-type host galaxies are structurally similar to well-assembled elliptical galaxies, following the luminosity-size relation of early-type galaxies. This indicates, most probably, that the process that has generated the blue colors has not strongly altered neither the luminosity (mass) and the effective radius of these galaxies. Taking into account this result, it seems that a mixed population, dominated by an underlying population of old stars, fits the observations better. This underlying population would reflect the population of the parent galaxy.

Our results are in excellent agreement with the results from the study of a large sample of type 1 and type 2 AGNs from the SDSS at lower redshift (Kauffmann et al. 2003). They



noted the existence of a population of *young bulge* galaxies (30% of their sample), in a state of post-starburst, and a population of even younger mergers (40% of their sample). Recent results by Jahnke et al. (2004) and Kotilainen & Falomo (2004) also found that low- $z$  host galaxies are bluer than field galaxies. While on the other hand, Dunlop et al. (2003) and Floyd et al. (2003) did not find evidence for distinctly blue colors in their sample of high-luminosity low- $z$  AGNs ( $z < 0.3$ ), their color range is less sensitive to young stellar populations at this redshift ( $R - K$ ), especially if there is an underlying population of old stars.

A possible explanation to the connection between nuclear and star formation activity in apparently normal elliptical galaxies could be an enrichment of gas produced by a merging process or the infall and concentration of gas produced by a minor interaction. Since the fraction of merger galaxies in our sample seems not to be remarkably larger than in inactive galaxies, the merger/interaction should have happened in a timescale long enough to enable the galaxy to relax morphologically before the current AGN activity.

#### ACKNOWLEDGMENTS

Support for the GEMS project was provided by NASA through grant number GO-9500 from the Space Telescope

Science Institute, which is operated by the Association of Universities for Research in Astronomy, Inc. for NASA, under contract NAS5-26555.

EFB and SFS acknowledge financial support provided through the European Community's Human Potential Program under contract HPRN-CT-2002-00316, SISCO (EFB) and HPRN-CT-2002-00305, Euro3D RTN (SFS).

CW was supported by a PPARC Advanced Fellowship.

SJ acknowledges support from the National Aeronautics and Space Administration (NASA) under LTSA Grant NAG5-13063 issued through the Office of Space Science.

DHM acknowledges support from the National Aeronautics and Space Administration (NASA) under LTSA Grant NAG5-13102 issued through the Office of Space Science.

The work of CYP was performed in part under contract with the Jet Propulsion Laboratory (JPL) funded by NASA through the Michelson Fellowship Program.

SFS wants to acknowledge Dr.M.M.Roth for supporting him in this work.

We would like to thanks the anonymous referee for his interesting and useful remarks that have improved the quality of this article.

#### REFERENCES

- Antonucci, R. 1993, *Ann. Rev. A&A*, 31, 473
- Bahcall, J. N., Kirhakos, S., Saxe, D. H., & Schneider, D. P. 1997, *ApJ*, 479, 642
- Bahcall, J. N., Kirhakos, S., & Schneider, D. P. 1995, *ApJ*, 450, 486
- Barton, E. J., Geller, M. J., & Kenyon, S. J. 2000, *ApJ*, 530, 660
- . 2003, *ApJ*, 582, 668
- Bell, E. F., & de Jong, R. S. 2001, *ApJ*, 550, 212
- Bell, E. F., McIntosh, D. H., Barden, M., Wolf, C., Caldwell, J. A. R., Rix, H., Beckwith, S. V. W., Borch, A., Häussler, B., Jahnke, K., Jogee, S., Meisenheimer, K., Peng, C., Sánchez, S. F., Somerville, R. S., & Wisotzki, L. 2004, *ApJ*, 600, L11
- Bergvall, N., Laurikainen, E., & Aalto, S. 2003, *A&A*, 405, 31
- Bruzual, G., & Charlot, S. 2003, *MNRAS*, 344, 1000
- Calzetti, D., Kinney, A. L., & Storchi-Bergmann, T. 1994, *ApJ*, 429, 582
- Canalizo, G., & Stockton, A. 2001, *ApJ*, 555, 719
- Chabrier, G. 2003, *PASP*, 115, 763
- Colbert, E. J. M., Baum, S. A., Gallimore, J. F., O'Dea, C. P., & Christensen, J. A. 1996, *ApJ*, 467, 551
- Collin, S., Combes, F., & Shlosman, I., eds. 2003, *ASP Conf. Ser. 290: Active Galactic Nuclei: From Central Engine to Host Galaxy*
- Constantin, A., Shields, J. C., Hamann, F., Foltz, C. B., Frederic, H. C., 2002, *ApJ*, 565, 50
- Corbin M.R., 2000, *ApJ*, 536, 73
- de Vaucouleurs, G., & Capaccioli, M. 1979, *ApJS*, 40, 699
- Dunlop, J. S., McLure, R. J., Kukula, M. J., Baum, S. A., O'Dea, C. P., & Hughes, D. H. 2003, *MNRAS*, 340, 1095
- Dunlop, J. S., Taylor, G. L., Hughes, D. H., & Robson, E. I. 1993, *MNRAS*, 264, 455
- Elvis, M., Wilkes, B. J., McDowell, J. C., Green, R. F., Bechtold, J., Willner, S. P., Oey, M. S., Polowski, E., Cutri, R., 1994, *ApJS*, 95, 1
- Faber, S. M., Dressler, A., Davies, R. L., Burstein, D., & Lynden-Bell, D. 1987, in *Nearly Normal Galaxies. From the Planck Time to the Present*, 175–183
- Falomo, R., Kotilainen, J., & Treves, A. 2001, *ApJ*, 547, 124
- Ferrarese, L., & Merrit, D. 2000, *ApJ*, 539, L9
- Floyd, D. J. E., Kukula, M. J., Dunlop, J. S., McLure, R. J., Miller, L., Percival, W. J., Baum, S. A., & O'Dea, C. P. 2003, *MNRAS* (submitted), (astro-ph/0308436)
- Freeman, K. C. 1970, *ApJ*, 160, 812
- Giavalisco
- Hamann, F., & Ferland, G., 1992, *ApJ*, 391, 53
- Hamann, F., & Ferland, G., 1993, *ApJ*, 418, 11
- Hamilton, T. S., Casertano, S., & Turnshek, D. A. 2002, *ApJ*, 576, 61
- Häring, N., & Rix, H.-W. 2004, *ApJ*, 604, 89
- Ho, L. C. 2003, in *ASP Conf. Ser. 290: Active Galactic Nuclei: From Central Engine to Host Galaxy*, 379
- Hutchings, J. B., & Neff, S. G. 1992, *AJ*, 104, 1
- . 1997, *AJ*, 113, 550
- Jahnke, K., Kuhlbrodt, B., & Wisotzki, L. 2004, *MNRAS*, (submitted), (astro-ph/0311123)
- Jahnke, K., Sánchez, S. F., Wisotzki, L., Barden, M., Bell, E. F., Beckwith, S. V. W., Borch, A., Caldwell, J. A. R., Häussler, B., Jogee, S., Meisenheimer, K., McIntosh, D. H., Peng, C., Rix, H., Somerville, R. S., & Wolf, C. 2004, *ApJ*, (submitted) (astro-ph/0403462)
- Jahnke, K., & Wisotzki, L. 2003, *MNRAS*, 346, 304
- Kauffmann, G., Heckman, T. M., Tremonti, C., Brinchmann, J., Charlot, S., White, S. D. M., Ridgway, S. E., Brinkmann, J., Fukugita, M., Hall, P. B., Ivezić, Ž., Richards, G. T., & Schneider, D. P. 2003, *MNRAS*, 346, 1055
- Kennicutt, R. C., Roettiger, K. A., Keel, W. C., van der Hulst, J. M., & Hummel, E. 1987, *AJ*, 93, 1011
- Kormendy, J. 1977, *ApJ*, 218, 333
- Kormendy, J., & Gebhardt, K. 2001, in *AIP Conf. Proc. 586: 20th Texas Symposium on relativistic astrophysics*, 363
- Kotilainen, J., Falomo, R., 2004, in *IAU Symposium No. 222, The Interplay among Black Holes, Stars and ISM in Galactic Nuclei*, Th.S. Bergmann, L.C. Ho & H.R. Schmitt, eds. (astro-ph/0404372)
- Larson, R. B., & Tinsley, B. M. 1978, *ApJ*, 219, 46
- Lee, M. G., & Hwang, N. 2000, *The Institute of Space and Astronautical Science Report SP*, 14, 131
- Lehnert, M. D., van Breugel, W. J. M., Heckman, T. M., & Miley, G. K. 1999, *ApJS*, 124, 11
- Lin, D.N.C., Pringle, J.E., & Riss, M.J., 1988, *ApJ*, 328, 103
- Magorrian, J., Tremaine, S., Richstone, D., Bender, R., Bower, G., Dressler, A., Faber, S. M., Gebhardt, K., Green, R., Grillmair, C., Kormendy, J., & Lauer, T. 1998, *AJ*, 115, 2285
- McLeod, K. K., & Rieke, G. H. 1994, *ApJ*, 420, 58
- . 1995, *ApJ*, 454, L77
- McLure, R. J., & Dunlop, J. S. 2002, *MNRAS*, 331, 795
- McLure, R. J., Dunlop, J. S., & Kukula, M. J. 2000, *MNRAS*, 318, 693
- McLure, R. J., Kukula, M. J., Dunlop, J. S., Baum, S. A., O'Dea, C. P., & Hughes, D. H. 1999, *MNRAS*, 308, 377
- Mihos, J. C., & Hernquist, L. 1996, *ApJ*, 464, 641
- Nolan, L. A., Dunlop, J. S., Kukula, M. J., Hughes, D. H., Boroson, T., & Jimenez, R. 2001, *MNRAS*, 323, 308
- Pagani, C., Falomo, R., & Treves, A. 2003, *ApJ*, 596, 830
- Peng, C. Y., Ho, L. C., Impey, C. D., & Rix, H. 2002, *AJ*, 124, 266
- Rix, H. W., Barden, M., Beckwith, S. V. W., Bell, E. F., Borch, A., Caldwell, J. A. R., Häussler, B., Jahnke, K., Jogee, S., McIntosh, D. H., Meisenheimer, K., Peng, C. Y., Sánchez, S. F., Somerville, R., Wisotzki, L., & Wolf, C. 2004, *ApJS* (in press), (astro-ph/0401427)
- Salpeter, E. E. 1955, *ApJ*, 121, 161
- Sánchez, S. F., & González-Serrano, J. I. 2003, *A&A*, 406, 435

- Sanders, D. B., Soifer, B. T., Elias, J. H., F., M. B., Matthews, K., Neugebauer, G., & Scoville, N. Z. 1988, *ApJ*, 325, 74
- Schade, D., Barrientos, L. F., & Lopez-Cruz, O. 1997, *ApJ*, 477, L17
- Schade, D., Boyle, B. J., & Letawsky, M. 2000, *MNRAS*, 315, 498
- Schlegel, D. J., Finkbeiner, D. P., & Davis, M. 1998, *ApJ*, 500, 525
- Schmidt, M. & Green, R. F., 1983, *ApJ*, 269, 352
- Sèrsic, J. L. 1968, in *Atlas de Galaxies Australes*; Vol. Book; Page 1
- Shapley, H., & Ames, A. 1932, in *Harvard Ann.*, 88
- Silk, J., & Rees, M. J. 1998, *A&A*, 331, L1
- Szokoly, G. P., Bergeron, J., Hasinger, G., Lehmann, I., Kewley, L., Mainieri, V., Nonino, M., Rosati, P., Giacconi, R., Gilli, R., Gilmozzi, R., Norman, C., Romaniello, M., Schreier, E., Tozzi, P., Wang, J. X., Zheng, W., & A., Z. 2004, *ApJS*, (submitted), (astro-ph/0312324)
- Taylor, G. L., Dunlop, J. S., Hughes, D. H., & Robson, E. I. 1996, *MNRAS*, 283, 930
- Urry, M. C., & Padovani, P. 1995, *PASP*, 107, 803
- van den Bergh, S., Abraham, R. G., Ellis, R. S., Tanvir, N. R., Santiago, B. X., & Glazebrook, K. G. 1996, *AJ*, 112, 359
- Wolf, C., Meisenheimer, K., Rix, H.-W., Borch, A., Dye, S., & Kleinheinrich, M. 2003, *A&A*, 401, 73
- Wolf, C., Meisenheimer, K., Kleinheinrich, M., Borch, A., Dye, S., Gray, M., Wisotzki, L., Bell, E. F., Rix, H.-W., Cimatti, A., Hasinger, G., Szokoly, G., 2004, *A&A*, in press
- Zaritsky, D. 1999, *AJ*, 118, 2824

## APPENDIX

## AGN IMAGES AND SURFACE BRIGHTNESS. NOTES ON INDIVIDUAL OBJECTS

Figure A10 shows the color images and surface brightness profiles for all the 15 objects in the sample. We present here detailed notes on individual objects:

**COMBO 34357:** This is the lowest redshift object of our sample. Its host is clearly resolved, being a blue spheroidal galaxy, without any clear trace of major disturbance. The residual image shows a clumpy structure near the very center that could be traces of an old merging event, although it is too close to the central area to be distinguished from a PSF subtraction effect.

**COMBO 41310:** A clearly resolved object. The host galaxy is as bright as the nucleus in both bands. The galaxy shows a clear spheroidal morphology, without evidence of recent interactions. There is a projected companion in the field of view.

**COMBO 52963:** A clearly resolved object. There is evidence for a recent or ongoing merging event, in the form of blue compact clumpy structures in both the residual and the original image. The host galaxy is of early morphological type.

**COMBO 36361:** A multiple system, comprising three major clumps of blue emission, and two nearby companions. There is clear evidence of a recent or ongoing merger. The morphological classification (late-type) is rather uncertain, due to the contamination from the nearby companions and substructures, some of them as bright as the host galaxy itself.

**COMBO 47615:** A spheroidal host galaxy. There are neither appreciable substructures in the residual image nor close companions.

**COMBO 50415:** Spheroidal host galaxy. There is a nearby blue and compact companion, and maybe blue low surface brightness substructure in the vicinity of the host galaxy.

**COMBO 44126:** The most compact and faintest host galaxy in our sample. The morphological classification (late-type) is uncertain due to the low brightness and size.

**COMBO 42601:** One of the biggest and brightest hosts of our sample. It is clearly classified as an early type galaxy, dominated by a large and blue spheroidal component. The residual image shows bright clumps and filaments, most probably due to recent star formation.

**COMBO 48284:** Big and bright host galaxy, clearly resolved. It shows a clearly spheroidal morphology, without traces of disturbance.

**COMBO 39432:** A compact spheroidal host galaxy. No irregularities in its morphology.

**COMBO 31898:** A compact spheroidal host galaxy. This is the reddest object of our sample, which can be appreciated in the color images.

**COMBO 15731:** One of the most beautiful objects of our sample. The host galaxy seems to be dominated by a central bulge, although both the residual and the host *restored* image show evidence of what could be two spiral arms. We have classified this object as an early-type galaxy, since it is clearly bulge dominated. It presents a nearby blue and compact companion, which may be interacting with the host. A possible bridge between the host and the companion is seen. It is difficult to clarify if the apparent arms are part of a real disk or structures produced by a recent collision.

**COMBO 50997:** The host galaxy of this object has been only detected in the F850LP-band. It is a compact spheroidal galaxy. It shows a close projected companion as big and bright as the host galaxy.

**COMBO 49298:** A clear late-type galaxy. The spiral arms are clearly seen in all the images.

**COMBO 43151:** This object is the highest redshift object of our sample. Its host galaxy has been detected only in the F850LP band, being a compact spheroidal galaxy, without evidence for disturbances.

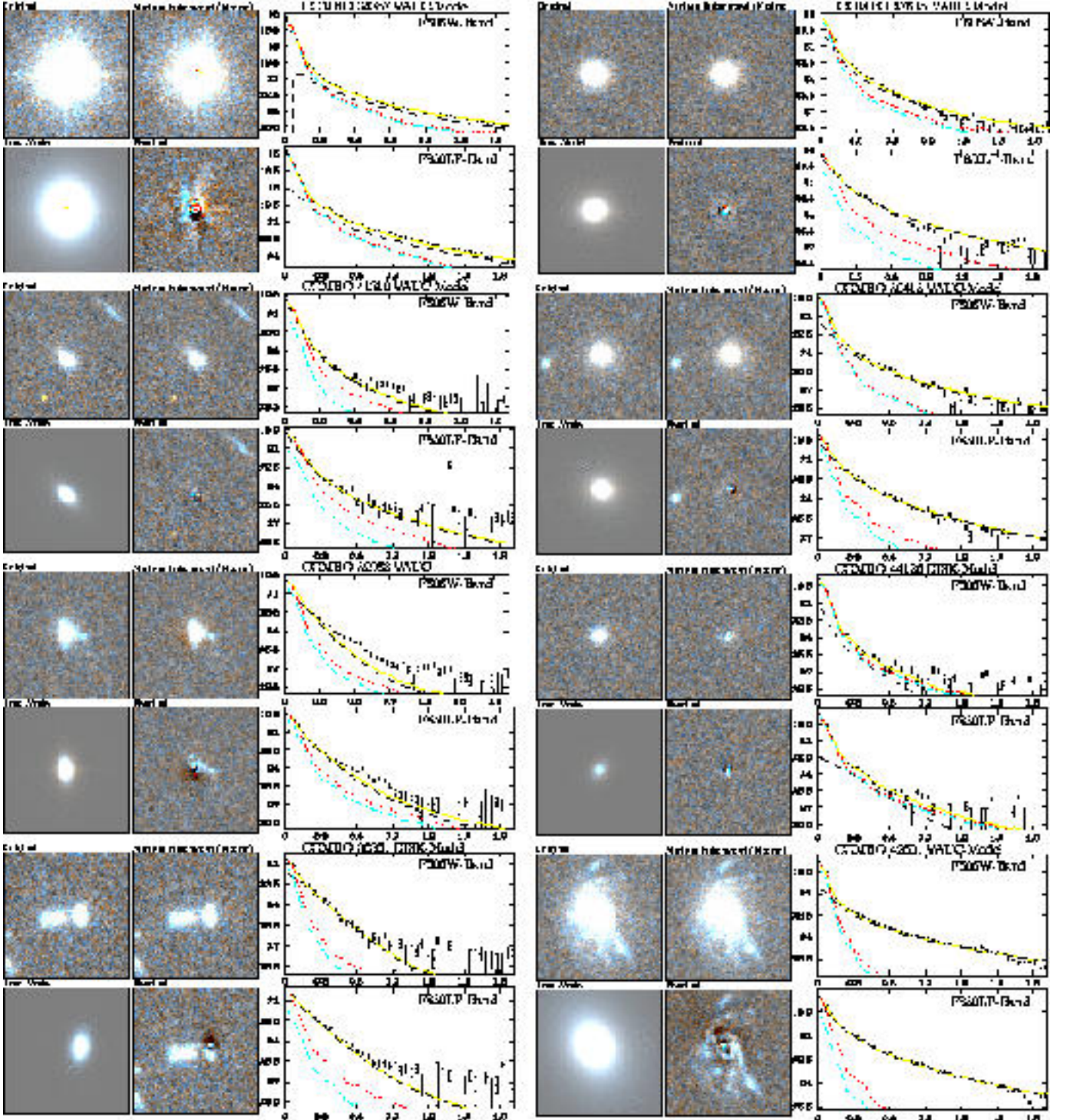


FIG. A10.— Each of the 15 panels, one per object, shows a color image created using the F606W and F850LP-band images for the original postage image of the object (top-left), the *restored* host (top-right), the host galaxy model (bottom-left), and residual image from the 2D fitting (bottom-right). To the right, we show the surface brightness profile of the object (black dots), together with the profile of the best fit (solid line, yellow), of the derived nucleus (dotted-dash line, blue), and of the best fitting host model (dashed line, black). For comparison, we have included the profiles of the *restored* host galaxy image, together with the profiles of the best-fit model and of the peak-scaled PSF subtraction (dotted line, red). All surface brightness profiles are in mag arcsec<sup>-2</sup>, the radii are in arcsec. The model fit is marked with a DISK label for an exponential profile, and with a VAUC for a de Vaucouleurs profile.

#### FROM OBSERVED TO REST-FRAME: EMPIRICAL $\kappa$ -CORRECTIONS

We calculated  $\kappa$ -corrections for the host galaxies by comparing them with galaxies of the same magnitude, redshift and colors from the COMBO-17 survey where spectral energy distributions (SEDs) are available for all objects. First, we derived the rest-frame  $U - V$  colors from the observed F606W - F850LP. For doing so we performed aperture photometry on the 4000



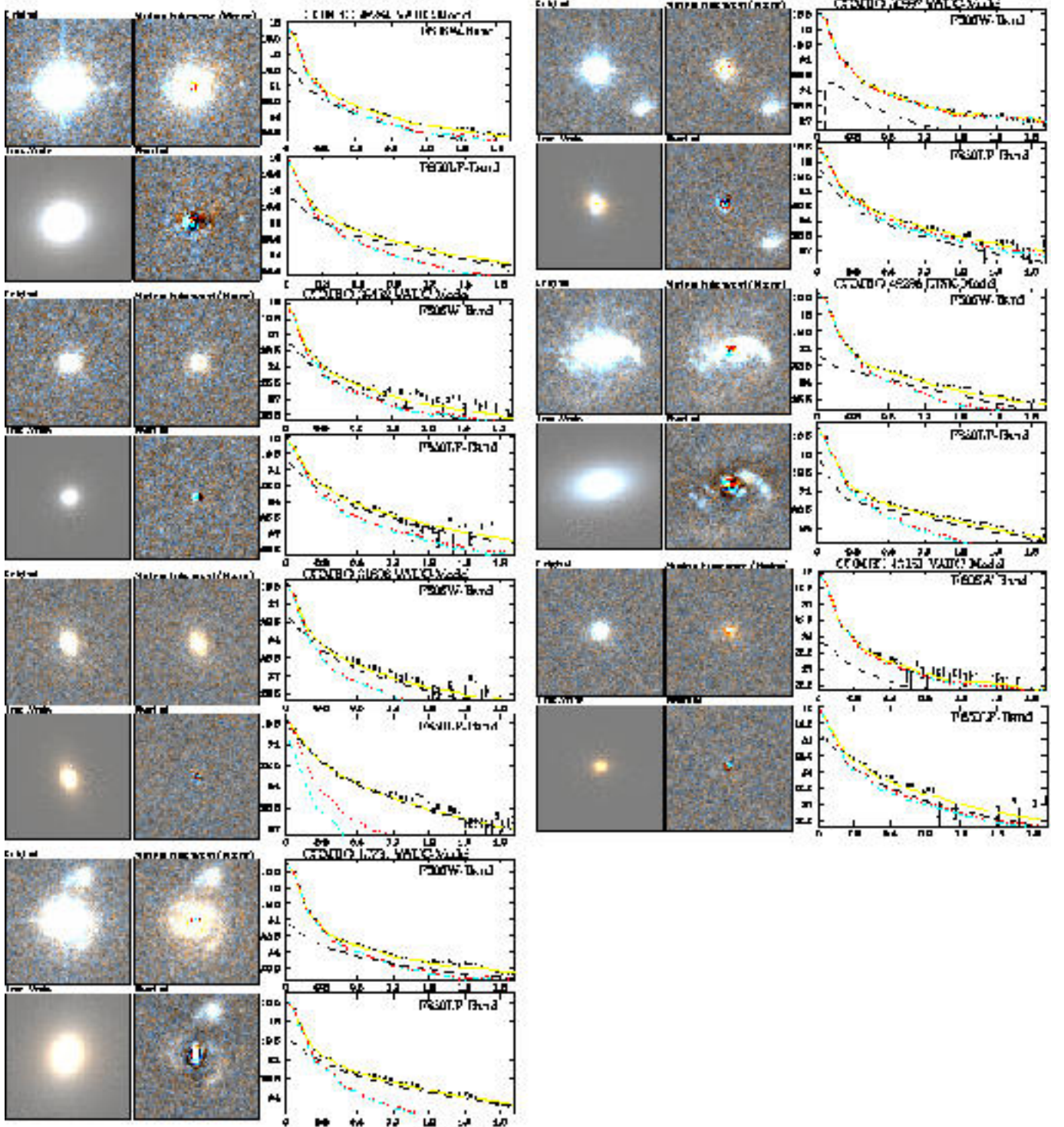


FIG. A10.— Continued

inactive galaxies in the GEMS field at the same redshift as our objects. We split this sample of galaxies in different redshift slices, each with a width of 0.02 and stepped by 0.01 in redshift. For each slice we found a good linear correlation between the observed  $F606W - F850LP$  and the rest-frame  $U - V$  colors. We computed linear regression solutions for the transformation

$$U - V = a(z) + b(z) (F606W - F850LP) \quad (B1)$$

for each slice separately, considering both forward and backward transformations and averaging the two. The rms dispersions were between  $0.12 - 0.22$  mag. This provided a grid of transformation coefficients  $a(z)$  and  $b(z)$  as shown in Fig. B11. We then fitted the  $a(z)$  and  $b(z)$  relations with high-order polynomials. Table B5 provides the polynomial coefficients needed to



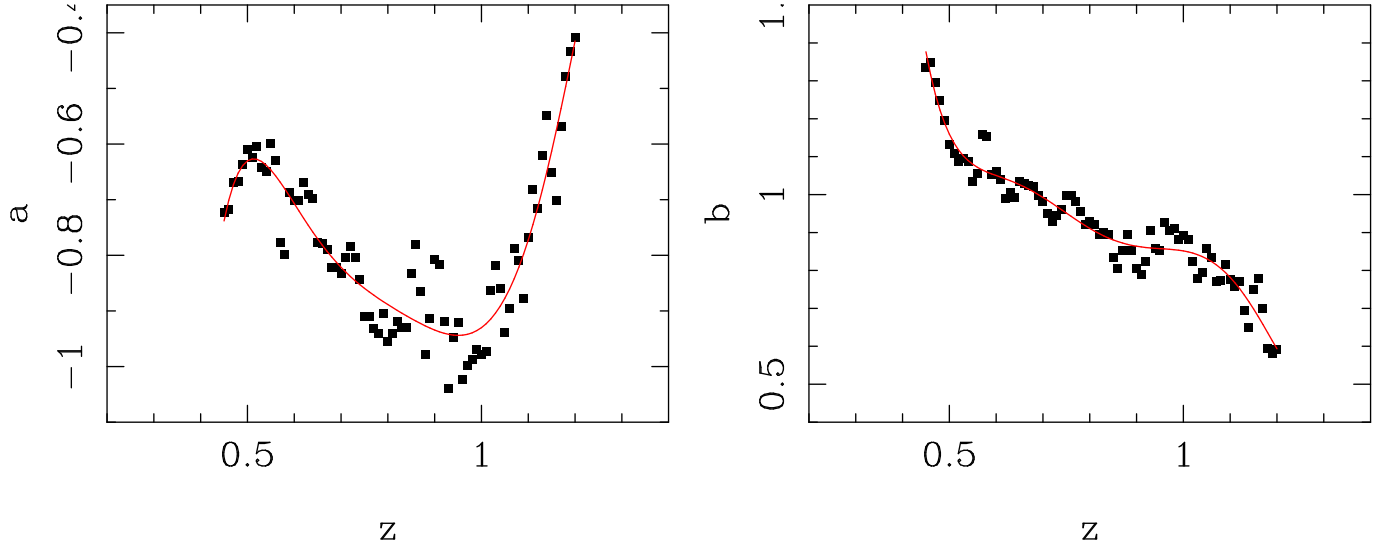


FIG. B11.— Distributions of the average  $a$  and  $b$  parameters of the linear regressions between the observed F606W-F850LP and the rest-frame  $U - V$  colors as a function of the redshifts, for the 4000 inactive galaxies in the GEMS field with COMBO-17 photometry. The solid lines show high-order polynomial fits to these distributions, the parameters of which can be found in Table B5.

TABLE B5

POLYNOMIAL COEFFICIENTS DESCRIBING THE REDSHIFT DEPENDENCE OF COLOR TRANSFORMATION PARAMETERS  $a = p_n(z)$  AND  $b = q_n(z)$ .

Order $n$	$p_n$	$q_n$
0	64.0375	71.9392
1	488.2067	538.3892
2	1529.8569	1676.0263
3	2503.5583	2730.2606
4	2262.2580	2450.3622
5	1070.2635	1148.4126
6	206.8062	219.5862

reconstruct the  $a$  and  $b$  parameters and perform the transformation at any redshift. In order to cross-validate this set of color transformations, we compared the rest-frame colors derived in this way with the original COMBO-17 colors, for the input sample of inactive galaxies (Figure B12). We found no systematic differences between both colors, and a spread of 0.16 mag (rms).

We then created a grid of COMBO-17  $U - V$  colors and redshifts, with a separation of 0.2 mag in colors and 0.02 in redshifts. Each grid box contained all objects within a color range of 0.6 mag and a redshift range of 0.1 around the central values of the box. For each grid box we found again a linear relation between the observed F850LP magnitude and the COMBO-17-based absolute  $V$  band magnitude

$$M_V = A(z; U - V) + B(z; U - V) \quad \text{F850LP} \quad (\text{B2})$$

where the regression coefficients however depend not only on redshift but also on the intrinsic color. Note that by using F850LP magnitudes at the mean redshift of our objects, we minimize this color term as we always sample the SED no far from the rest-frame  $V$  band. The rms dispersions of the  $M_V$  values around the linear regression fits are around 0.15–0.22 mag. We fitted the regression parameters with 2nd order polynomials as a function of  $z$ , separately for each color range. Table B6 provides the coefficients required to derive the  $A$  and  $B$  regression parameters. Again, we cross-validated this set of transformations by applying it to the COMBO-17 inactive galaxies, finding no systematic differences between the two ways to estimate  $M_V$ , and a spread of 0.28 mag (Figure B13).

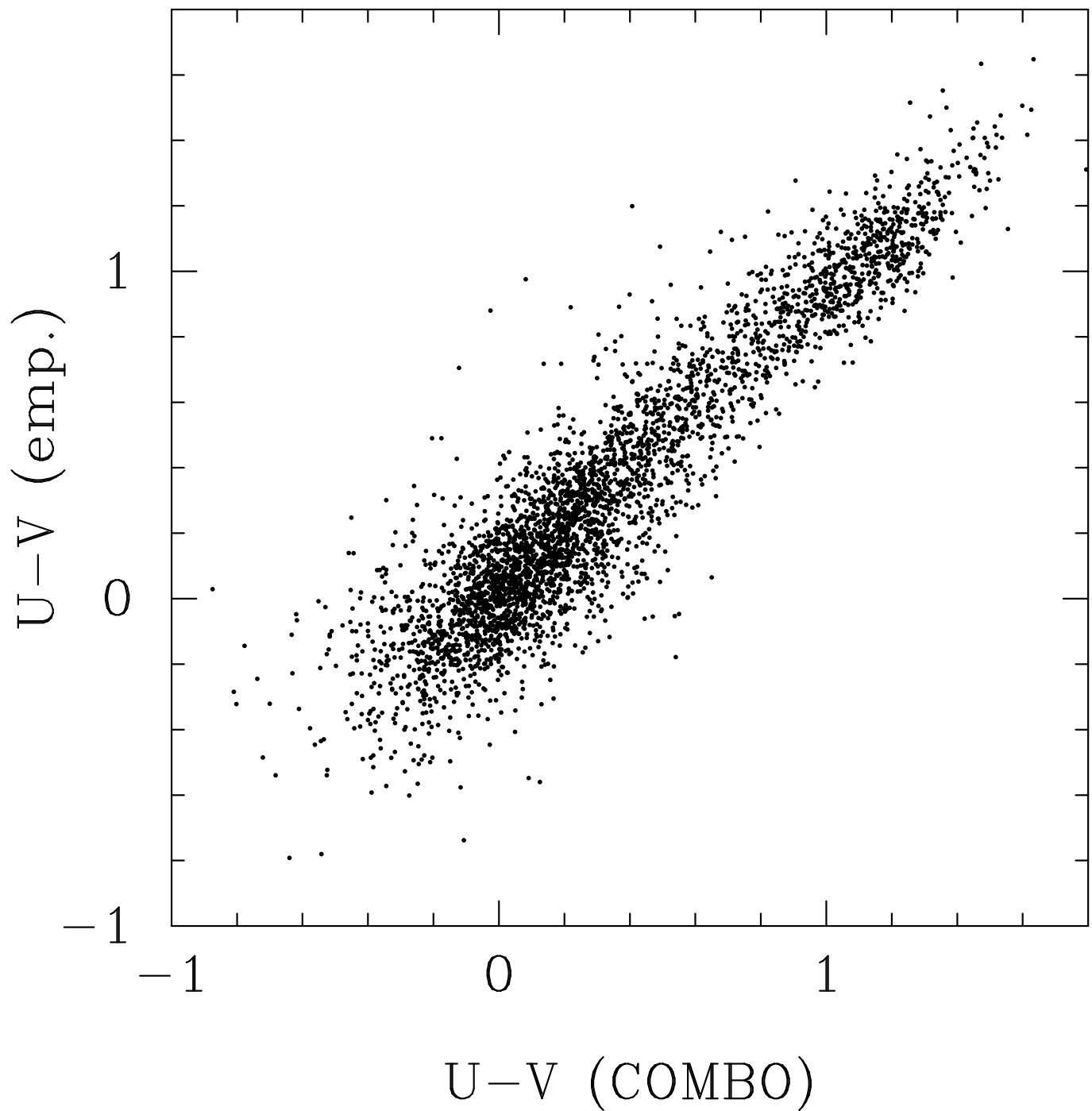


FIG. B12.— Comparison between rest-frame  $U-V$  colors of inactive galaxies from COMBO-17 multiband photometry and the  $U-V$  values estimated from observed GEMS F606W-F850LP, using the transformation described in the text.

TABLE B6

POLYNOMIAL COEFFICIENTS DESCRIBING THE REDSHIFT DEPENDENCE OF OBSERVED TO ABSOLUTE MAGNITUDE TRANSFORMATION PARAMETERS  
 $A = P_n(z)$  AND  $B = Q_n(z)$ , SEPARATELY FOR DIFFERENT REST-FRAME COLORS.

U	V	Order n	$P_n$	$Q_n$	U	V	Order n	$P_n$	$Q_n$
0.4		0	36.3631	0.8845	0.6		0	37.8007	0.9602
0.4		1	26.1132	0.9650	0.6		1	2.5629	0.1072
0.4		2	20.0688	0.8527	0.6		2	2.5713	0.1569
0.2		0	38.9592	1.0106	0.8		0	28.9003	0.5637
0.2		1	11.0029	0.2691	0.8		1	28.2281	1.0473
0.2		2	7.7105	0.2934	0.8		2	13.3033	0.5641
0.0		0	34.9194	0.8240	1.0		0	38.8294	1.0262
0.0		1	16.9380	0.5508	1.0		1	4.4406	0.4684
0.0		2	9.3486	0.3781	1.0		2	12.5859	0.6327
0.2		0	34.0425	0.7915	1.2		0	44.8231	1.3100
0.2		1	17.9921	0.5816	1.2		1	20.8241	1.2308
0.2		2	9.5968	0.3823	1.2		2	22.9941	1.1100
0.4		0	33.2426	0.7501	1.4		0	57.9184	1.9331
0.4		1	16.3457	0.5202	1.4		1	55.7256	2.8866
0.4		2	6.5599	0.2537	1.4		2	44.3401	2.1188

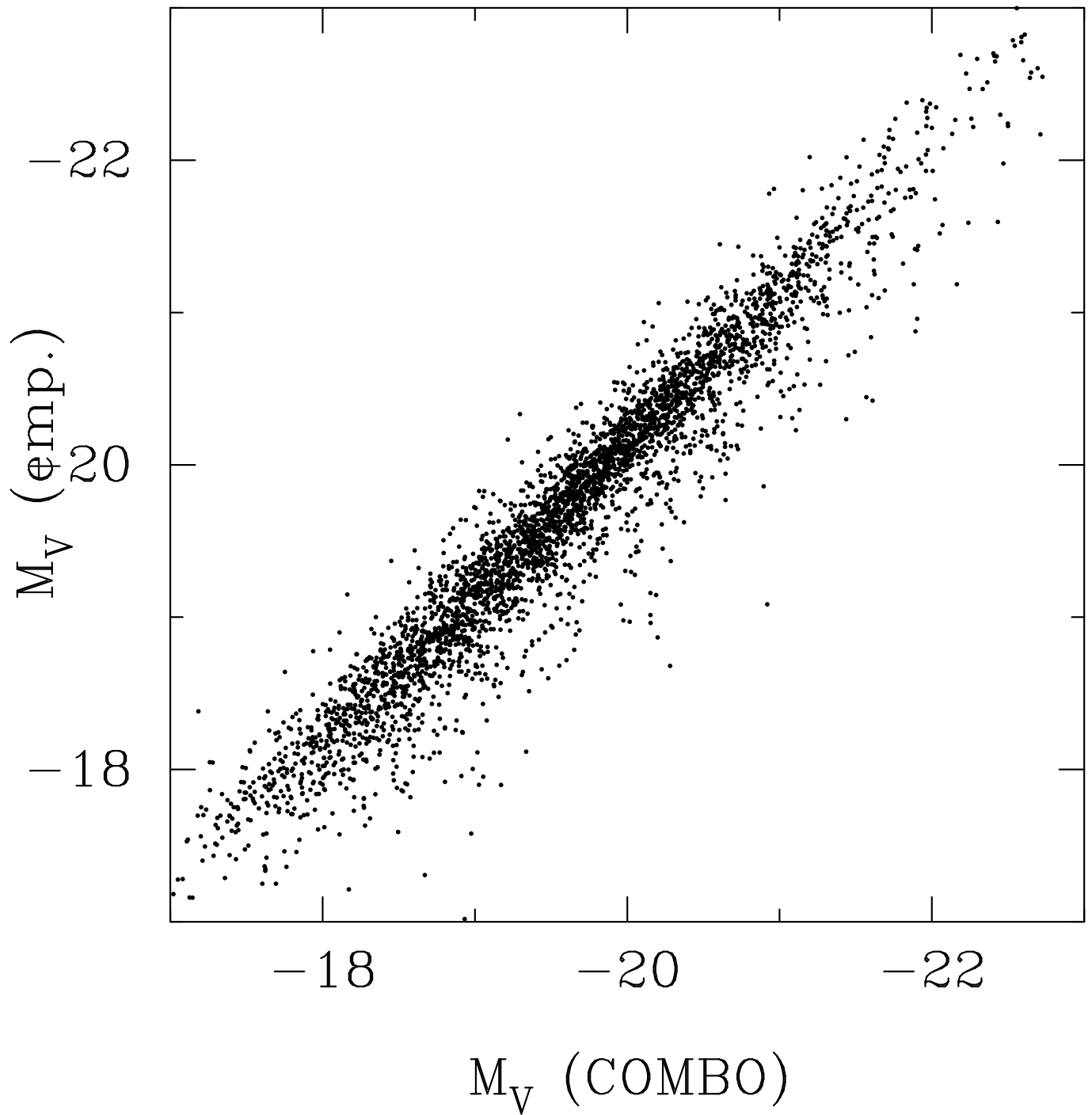


FIG. B13.— Comparison between absolute magnitudes  $M_V$  of inactive galaxies from COMBO-17 multiband photometry and color-dependent  $M_V$  estimated from observed GEMS F850LP, using the transformation described in the text.